Technical note: A high-resolution inverse modelling technique for estimating surface CO₂ fluxes based on the NIES-TM - FLEXPART coupled transport model and its adjoint.

Shamil Maksyutov[1], Tomohiro Oda[2], Makoto Saito[1], Rajesh Janardanan[1], Dmitry Belikov[1,3], Johannes W. Kaiser[4], Ruslan Zhuravlev[5], Alexander Ganshin[5], Vinu K. Valsala[6], Arlyn Andrews[7], Lukasz Chmura[8], Edward Dlugokencky[7], László Haszpra[9], Ray L. Langenfelds[10], Toshinobu Machida[1], Takakiyo Nakazawa[11], Michel Ramonet[12], Colm Sweeney[7], Douglas Worthy[13]

[1]National Institute for Environmental Studies, Tsukuba, Japan
[2]NASA Goddard Space Flight Center, Greenbelt, MD, USA/Universities Space Research Association, Columbia, MD, USA
[3]now at Chiba University, Chiba, Japan
[4]Deutscher Wetterdienst, Offenbach, Germany
[5]Central Aerological Observatory, Dolgoprudny, Russia
[6]Indian Institute for Tropical Meteorology, Pune, India
[7]Earth System Research Laboratory, NOAA, Boulder, CO, USA
[8]AGH University of Science and Technology, Krakow, Poland
[9]Research Centre for Astronomy and Earth Sciences, Sopron, Hungary
[10]Climate Science Centre, CSIRO Oceans and Atmosphere, Aspendale, VIC, Australia
[11]Tohoku University, Sendai, Japan
[12]Laboratoire des Sciences du Climat et de l'Environnement, LSCE-IPSL, Gif-sur-Yvette, France
[13]Environment and Climate Change Canada, Toronto, Canada

Correspondence to: S. Maksyutov (shamil@nies.go.jp)

Abstract

We developed a high-resolution surface flux inversion system based on the global Lagrangian-Eulerian coupled tracer transport model composed of National Institute for Environmental Studies Transport Model (NIES-TM) and FLEXible PARTicle dispersion model (FLEXPART). The inversion system is named NTFVAR (NIES-TM-FLEXPART-variational) as it applies variational optimisation to estimate surface fluxes. We tested the system by estimating optimized corrections to natural surface CO_2 fluxes to achieve best fit to atmospheric CO_2 data collected by the global in-situ network, as a necessary step towards capability of estimating anthropogenic CO_2 emissions. We employ the Lagrangian particle dispersion model (LPDM) FLEXPART to calculate the surface flux footprints of CO_2 observations at a $0.1° \times 0.1°$ spatial

resolution. The LPDM is coupled to a global atmospheric tracer transport model (NIES-TM). Our inversion technique uses an adjoint of the coupled transport model in an iterative optimization procedure. The flux error covariance operator is being implemented via implicit diffusion. Biweekly flux corrections to prior flux fields were estimated for the years 2010-2012 from in-situ CO_2 data included in the Observation Package (ObsPack) dataset. High-resolution prior flux fields were

5 prepared using Open-Data Inventory for Anthropogenic Carbon dioxide (ODIAC) for fossil fuel combustion, Global Fire Assimilation System (GFAS) for biomass burning, the Vegetation Integrative SImulator for Trace gases (VISIT) model for terrestrial biosphere exchange and Ocean Tracer Transport Model (OTTM) for oceanic exchange. The terrestrial biospheric flux field was constructed using a vegetation mosaic map and separate simulation of CO_2 fluxes at daily time step by the VISIT model for each vegetation type. The prior flux uncertainty for terrestrial biosphere was scaled

10 proportionally to the monthly mean Gross Primary Production (GPP) by the Moderate Resolution Imaging Spectroradiometer (MODIS) MOD17 product. The inverse system calculates flux corrections to the prior fluxes in the form of a relatively smooth field multiplied by high-resolution patterns of the prior flux uncertainties for land and ocean, following the coastlines and vegetation productivity gradients. The resulting flux estimates improve fit to the observations at continuous observations sites, reproducing both the seasonal variation and short-term concentration variability, including

15 high CO_2 concentration events associated with anthropogenic emissions. The use of high-resolution atmospheric transport in global CO_2 flux inversion has the advantage of better resolving the transport from the mix of the anthropogenic and biospheric sources in densely populated continental regions and shows potential for better separation between fluxes from terrestrial ecosystems and strong localised sources such as anthropogenic emissions and forest fires. Further improvements in the modelling system are needed as the posterior fit is better than that by the National Oceanic and Atmospheric

20 Administration (NOAA) CarbonTracker only for a fraction of the monitoring sites, mostly at coastal and island locations experiencing mix of background and local flux signals.

1   Introduction

Inverse modelling of the surface fluxes is implemented by using chemical transport model simulations to match

25 atmospheric observations of greenhouse gases. CO_2 flux inversions studies started from addressing large scale flux distributions (Enting and Mansbridge, 1989; Tans et al., 1990; Gurney et al., 2002; Peylin et al., 2013 and others) using background monitoring data and global transport models at low and medium resolutions targeting extraction of the information on large and highly variable fluxes of carbon dioxide from terrestrial ecosystems and oceans. Merits of improving the resolutions of global transport simulations to 9-25 km have been also discussed by previous studies, such as

30 Agusti-Panareda et al. (2019) and Maksyutov et al. (2008). However, global inverse modelling studies have never been conducted at these spatial resolutions. On the other hand, regional scale fluxes, such as national emissions of non-CO_2

greenhouse gases (GHGs), have been estimated using inverse modelling tools relying on regional (mostly Lagrangian) transport algorithms capable of resolving surface flux contributions to atmospheric concentrations at resolutions from 1 to 100 km (Vermeulen et al., 1999; Manning et al., 2011; Stohl et al., 2009; Rodenbeck et al., 2009; Henne et al., 2016; He et al., 2018; Schuh et al., 2013; Lauvaux et al., 2016 and others). Extension of the regional Lagrangian inverse modelling

5   to the global scale based on combination of three-dimensional (3-D) global Eulerian model and Lagrangian model have been implemented in several studies (Rugby et al., 2011; Zhuravlev et al., 2013; Shirai et al., 2017), which demonstrated an enhanced capability of resolving the regional and local concentration variability driven by fine scale surface emission patterns, while using inverse modeling schemes relying on regional and global basis functions that yield concentration responses of regional fluxes at observational sites. A disadvantage of using regional basis functions in inverse modeling is

10   the flux aggregation errors as noted by Kaminski et al. (2001). This is addressed by developing grid-based inversion schemes based on variational assimilation algorithms that yield flux corrections that are not tied to aggregated flux regions (Rodenbeck et al., 2003; Chevallier et al., 2005; Baker et al., 2006, and others). In order to implement a grid-based inversion scheme suitable for optimizing surface fluxes using a high-resolution atmospheric transport capability of the Lagrangian model, an adjoint of a coupled Eulerian-Lagrangian model is needed, such as one reported by Belikov et al. (2016).

15   In this study, we applied an adjoint of the coupled Eulerian-Lagrangian transport model, which is a revised version of Belikov et al. (2016), to the problem of surface flux inversion based on coupled transport model with a spatial resolution of the Lagrangian model 0.1° longitude-latitude. While global higher resolution transport runs can be tried with coupled Eulerian-Lagrangian models (e.g. Ganshin et al., 2012), the choice of the model resolution in our inversion system is dictated mostly by the availability of the prior surface CO_2 fluxes.

20   A practical need for running high-resolution atmospheric transport simulations at global scale is currently driven by expanding GHG observing capabilities towards quantifying anthropogenic emissions by observing CO_2 at the vicinity of emission sources (Nassar et al., 2017; Lauvaux et al., 2020), including observations in both background and urban sites, with tall towers, commercial airplanes, and satellites. At the same time, the focus of inverse modeling is evolving towards studies of the anthropogenic emissions, with a target of making better estimates of regional and national emissions in

25   support of national and regional GHG emission reporting and control measures (Manning et al., 2011; Henne et al., 2016; Lauvaux et al., 2020). In that context, global-scale high-resolution inverse modeling approaches have advantage in closing global budgets, while regional and national scale inverse modeling approaches with limited area models require boundary conditions normally provided by global model simulations with optimized fluxes. Often there is an additional degree of freedom introduced by allowing corrections to the boundary concentration distribution to improve a fit at the observation

30   sites (Manning et al., 2011). As a result, the global total of regional emission estimates does not necessarily match the balance constrained by global mean concentration trends. A global coupled Eulerian-Lagrangian model (e.g. Ganshin et

al., 2012), has potential for addressing both the objectives, that is closing the global balance and operating at range of scales from a single city (Lauvaux et al., 2016) to large country or continental scale. Here we report developing a high-resolution inverse modeling technique suitable for application at a broad range of spatial scales and apply it to the problem of estimating the distribution of CO_2 fluxes over the globe that provides best fit to the observations. In separate studies, the same inversion system was applied to inverse modeling of methane emissions (Wang et al., 2019; Janardanan et al., 2020). The objective of this study is optimizing the natural CO_2 fluxes in order to provide a background for estimating the fossil CO_2 emissions where the advantage of high-resolution approach is more evident. The paper is composed as follows: this Section 1 provides Introduction; Section 2, the transport model and its adjoint; Section 3 introduces the Prior fluxes, observational dataset, and gridded flux uncertainties; Section 4 gives the formulation of the inverse modeling problem and numerical solution; Section 5 presents simulation results and discussion, which is followed by the Summary and Conclusions.

2   The coupled tracer transport model, its adjoint and the implementation

For simulation of the CO_2 transport in the atmosphere we used a coupled Eulerian-Lagrangian model NIES-TM-FLEXPART, which is a further modification of the model described by Belikov et al. (2016). Coupled transport model is computationally more efficient in comparison to the Eulerian model operating at the same spatial resolution. It was confirmed by Belikov et al, (2016) that coupled model with Lagrangian model run at resolution of $1°×1°$ performs similarly when coupled with Eulerian model at either $1.25°×1.25°$ or $2.5°×2.5°$ resolution, and only can see performance degradation when using $10°×10°$ resolution Eulerian model. The coupled model combines NIES-TM v08.1i with horizontal resolution of $2.5° × 2.5°$ and 32 hybrid-isentropic vertical levels (Belikov et al., 2013) and FLEXPART model v.8.0 (Stohl et al., 2005) run in backward mode with surface flux resolution of $0.1° × 0.1°$. Both models use the Japan 25-year reanalysis (JRA-25)/JMA Climate Data Assimilation System (JCDAS) meteorology (Onogi et al., 2007), with 40 vertical levels interpolated to a $1.25° × 1.25°$ grid. The use of low-resolution wind fields for high resolution transport is better justified for cases of nearly geostrophic flow over flat terrain, as discussed by Ganshin et al., (2012). It should be useful in the future to adapt this modeling framework to using reanalyses recently made available at $0.25°$-$0.3°$ resolution, even if the tests with higher resolution winds by Ware et al., (2019) did not show large improvement over lower resolution.

The coupled transport model was derived from the Global Eulerian-Lagrangian Coupled Atmospheric transport model (GELCA) (Ganshin et al., 2012; Zhuravlev et al., 2013; Shirai et al., 2017). To facilitate model application in our iterative inversion algorithm, all the components of the model – Eulerian model and the coupler are integrated in one executable (online coupling) as described in Belikov et al., (2016), while the original GELCA model implements Eulerian and

Lagrangian components sequentially, and then applies the coupler (off-line coupling). The changes in the current version with respect to the version presented by Belikov et al. (2016) include an adjoint code derivation for model components using the adjoint code compiler Tapenade (Hascoet and Pascual, 2013), instead of using the TAF compiler (Giering and Kaminski, 2003). Additionally, the indexing and sorting algorithms for the transport matrix were revised to allow an efficient memory use for processing large matrices of LPDM-driven responses to surface fluxes arising in the case of high-resolution surface fluxes and large number of observations, especially when using satellite data. A manually derived adjoint of the NIES-TM v08.1i is used as in Belikov et al. (2016), due to its computational efficiency. In the version of the model that includes manually coded adjoint, only the second order van Leer algorithm (van Leer, 1977) is implemented, as opposed to third order algorithm typically used in forward model (Belikov et al., 2013).

3   Prior fluxes, flux uncertainties and observations

Prior CO_2 fluxes, were prepared as a combination of monthly-varying fossil fuel emissions by the Open-Data Inventory for Anthropogenic Carbon dioxide (ODIAC), available at a global 30 arc second resolution (Oda et al., 2018), ocean-atmosphere exchange by the Ocean Tracer Transport Model (OTTM) 4D-var assimilation system, available at a 1° resolution (Valsala and Maksyutov, 2010), daily CO_2 emissions by biomass burning by Global Fire Assimilation System (GFAS) dataset provided by Copernicus services at a 0.1° resolution (Kaiser et al., 2012), and daily varying climatology of terrestrial biospheric CO_2 exchange simulated by optimized Vegetation Integrative SImulator for Trace gases (VISIT) model (Ito, 2010; Saito et al., 2014). Figure 1 presents samples of the four prior flux components (fossil, vegetation, biomass burning and ocean) used in the forward simulation.

3.1   Emissions from fossil fuel

For fossil fuel CO_2 emissions (emissions due to of fossil fuel combustion and cement manufacturing) we used ODIAC data product (Oda and Maksyutov, 2011, 2015; Oda et al., 2018) at 0.1° × 0.1° resolution on monthly basis. The version 2016 of the ODIAC-2016 data product (ODIAC2016, Oda et al., 2018) is based on global and national emission estimates and monthly estimates made at monthly resolution by the Carbon Dioxide Information Analysis Center (CDIAC) (Boden et al., 2016; Andres et al., 2011). For spatial disaggregation it uses the emission data for powerplant emissions by the CARbon Monitoring and Action (CARMA) database (Wheeler and Ummel, 2008), while the rest of the national total emissions on land were distributed using spatial patterns provided by night-time lights data collected by the Defence Meteorological Satellite Program (DMSP) satellites (Elvidge et al., 1999). The ODIAC fluxes were aggregated to a 0.1° resolution from

the high-resolution ODIAC data. The ODIAC emission product is suitable for this type of studies because the global total emission is constrained by updated estimates while providing a high-resolution emission estimate. Thus, it can be applied to carbon budget problems across different scales.

3.2   Terrestrial biosphere fluxes

CO_2 fluxes by the terrestrial biosphere at a resolution of 0.1° were constructed using a vegetation mosaic approach, combining the vegetation map data by synergetic land cover product (SYNMAP) dataset (Jung et al., 2006), available at a 30 arc second resolution, with terrestrial biospheric CO_2 exchanges simulated by optimized VISIT model (Saito et al., 2014) for each vegetation type in every 0.5° grid at daily time step. The area fraction of each vegetation type is derived from SYNMAP data for each 0.1° grid. The CO_2 net ecosystem exchange (NEE) fluxes on 0.1° grid were prepared by combining the vegetation type-specific fluxes with vegetation area fraction data on 0.1° grid. By averaging the daily flux data for period of 2000-2005 the flux climatology was derived for use in the recent years (after 2010), when the VISIT model simulation based on JRA-25-JCDAS reanalysis data is not available. Although the use of climatology in place of original fluxes degrades the prior, the posterior fluxes show significant departures from prior, thus reducing the impact of missing the prior variations. The diurnal cycle was not resolved as it requires producing additionally the gross primary production and ecosystem respiration. To estimate the effect of excluding the diurnal cycle in the prior fluxes, for our selected time of sampling the observations, we compared CO_2 concentrations simulated with diurnally varying fluxes at hourly time step with those made with daily mean fluxes produced by SiB model for 2002-2003 (Denning et al, 1996) as used in Transcom continuous intercomparison (Law et al, 2008). The results show that, for background monitoring sites the difference is not significant (below 0.1 ppm), same result as by Denning et al, (1996). For continental sites, the difference between the two simulations were combined into four seasonal values, and the data for the season with largest difference were shown in Figure A1. Positive bias by simulation with daily constant flux with respect to diurnally varying fluxes is in the order of 0.5 to 1 ppm, and it is larger during middle of the growing season. Inclusion of the diurnally varying fluxes in place of daily mean has potential to change seasonality of posterior fluxes by inversion in favourable direction, as there are regions where flux seasonality is somewhat stronger than expected (Section 5.2).

3.3   Emissions from biomass burning

Daily biomass burning CO_2 emissions by Global Fire Assimilation System (GFAS) dataset relies on assimilating Fire Radiative Power (FRP) observations from the MODIS instruments onboard the Terra and Aqua satellites (Kaiser et al., 2012). The fire emissions at 0.1° resolution are calculated from FRP with land cover-specific conversion factors compiled

from a literature survey. The GFAS system adds corrections for observation gaps in the observations, and filters spurious FRP observations of volcanoes, gas flares and other sources. The fluxes are input to the model at the surface, which may lead to underestimation of injection height for strong burning events and occasional overestimation of biomass burning signal simulated at surface stations.

3.4   Oceanic exchange flux

The air-sea CO_2 flux component for the flux inversion used an optimized estimate of oceanic CO_2 fluxes by Valsala and Maksyutov (2010). The dataset is constructed with a variational assimilation of the observed partial pressure of surface ocean CO_2 (pCO_2) available in Takahashi et al. (2017) database into the OTTM (Valsala et al., 2008), coupled with a simple one-component ecosystem model. The assimilation consists of a variational optimization method which minimizes the model to observation differences in the surface ocean dissolved inorganic carbon (DIC) (or pCO_2) within two-month time window. The OTTM model fluxes produced on a $1° \times 1°$ grid at monthly time step are interpolated to a $0.1° \times 0.1°$ grid, taking into account, the land fraction map derived from 1 km resolution MODIS landcover product.

3.5   Flux uncertainties for land and ocean.

CO_2 flux uncertainties are needed for both land and ocean. Climatological, monthly-varying flux uncertainties for land were set to 20% of MODIS gross primary productivity (GPP) by MOD17A2 product available on a $0.05°$ grid at monthly resolution (Running et al., 2004). Oceanic flux uncertainties are assigned based on the standard deviation of the OTTM assimilated flux from climatology by Takahashi et al. (2009), plus the monthly variance of the interannually-varying OTTM fluxes (Valsala and Maksyutov, 2010), with a minimum value of 0.02 $gCm^{-2}day^{-1}$, in the same way as in the lower spatial resolution inverse model by Maksyutov et al. (2013). Oceanic flux uncertainties were first estimated on a $1° \times 1°$ resolution at monthly time step, and then interpolated to a $0.1° \times 0.1°$ grid, with the same procedure as for the oceanic fluxes.

3.6   Atmospheric CO_2 observations.

We used CO_2 observation data distributed as the ObsPack-CO_2 GLOBALVIEWplus v2.1 (Cooperative Global Atmospheric Data Integration Project, 2016). The data from the flask sites were used as average concentration for a pair of flasks. Afternoon (15:00 to 16:00 local time) average concentrations were used for continuous observations over land and for remote background observation sites. For the continuous mountain top observations, we used early morning observations (05:00 to 06:00 local time). Geographical local time is used, as defined by UTC time with longitude dependent offset. The list of the observation locations, with ObsPack site ID, site names, data providers and data references appear in

the Table A1 in the Appendix, accompanied by a site map on Figure A2. Aircraft observational data collected by NOAA Aircraft Program at Briggsdale, Colorado (CAR), Cape May, New Jersey (CMA), Dahlen, North Dakota (DND), Homer, Illinois (HIL), Worcester, Massachusetts, (NHA), Poker Flats, Alaska (PFA), Rarotonga, (RTA), Charleston, South Carolina (SCA), Sinton, Texas (TGC) (Sweeney et al., 2015), and by the CONTRAIL project over West Pacific (CON) (Machida et al., 2008) were grouped into averages for each 1 km altitude bin, altitude counted from sea level. Within the 1 km altitude range, the average value of both concentration and the altitude are taken. Aircraft observations were not assimilated, only intended for use in the validation of the results.

4   Inverse modelling algorithm

4.1   Flux optimization problem

Inverse problem of atmospheric transport is formulated by Enting (2002) as finding the surface fluxes that minimize misfit between transport model simulation $y_f + H \cdot (x_p + x)$ and the vector of observations y, where y_f is forward simulation without the surface fluxes, x_p is known prior flux, x is unknown flux correction, and H represents transport model. The equation $y = y_f + H \cdot (x_p + x)$ has to be solved for unknown flux correction x, and x is solved for at the transport model grid scale (Kaminski et al., 2001). By introducing the residual misfit vector $r = y - (y_f + H \cdot x_p)$, the problem can be formulated as minimizing a norm of difference $(r - H \cdot x)$ weighted by the data uncertainties. As the observation data alone are not sufficient to uniquely define the solution x, additional regularization is required. By introducing additional constraints on the amplitude and smoothness of the solution, the inverse modelling problem is formulated (Tarantola, 2005) as solving for optimal value of vector x at the minimum of a cost function $J(x)$:

$$J(x) = \frac{1}{2}(H \cdot x - r)^T \cdot R^{-1} \cdot (H \cdot x - r) + \frac{1}{2}x^T \cdot B^{-1} \cdot x \tag{1}$$

where x is optimised flux, R is a covariance matrix for observations and B is a covariance matrix for surface fluxes. By introducing a decomposition of B as $B = L \cdot L^T$ (construction of matrix L explained in detail in Section 4.2) and a variable substitution $x = L \cdot z$ the second term in Eq. (1) is simplified. At the same time, by assuming that R can be decomposed into $R = \sigma^T \cdot \sigma$, where σ is a vector of data uncertainties, and introducing expressions $b = \sigma^{-1} \cdot (r - H \cdot x)$, and $A = \sigma^{-1} \cdot H \cdot L$, the new form of Eq. (1) is introduced:

$$J(z) = \frac{1}{2}((A \cdot z - b)^T(A \cdot z - b) + z^T \cdot z) \tag{2}$$

The solution minimizing $J(z)$ can be obtained by forcing the derivative $\partial J(z)/\partial z = A^T(A \cdot z - b) + z$ to zero, which results in

$$(A^T A + I) \cdot z = A^T b \tag{3}$$

An optimal solution z at the minimum of the cost function $J(z)$ is found iteratively with the Broyden–Fletcher–Goldfarb–Shanno (BGFS) algorithm (Broyden, 1969; Nocedal, 1980), as implemented by Gilbert and Lemarechal (1989). The method requires ability to accurately estimate the cost function $J(z)$ and its gradient $A^T(A \cdot z - b) + z$, and has modest memory storage demands. Given the solution z, flux correction vector x is then found by reversing variable substitution as $x = L \cdot z$.

The convergence of the solution may be affected by accuracy of the adjoint. The result of duality test defined as norm of difference between NIES-TM-FLEXPART forward and adjoint modes estimated as $(< y, H \cdot x > - < H^T \cdot y, x >)/(< y, H \cdot x >)$ was found to be in the order of 10^{-9}, while for Lagrangian component based on receptor sensitivity matrices prepared with FLEXPART, it is about 10^{-15} when double precision is used in calculations, same as in (Belikov et al., 2016). The formulation of the minimization problem as presented by Eq. (2) is convenient for the derivation of the flux uncertainties, as it is possible to solve Eq. (3) via the truncated singular value decomposition (SVD) and estimate regional flux uncertainties based on derived singular vectors (Meirink et al., 2008). Alternatively, as mentioned by Fisher and Courtier (1995) it is also possible to use the flux increments derived at each iteration of the BFGS algorithm in place of the singular vectors. Although we did not use SVD for constructing the posterior covariances in this study, we tested solving the optimisation problem with SVD. We derived SVD of $A^T A$ using a code by Wu and Simon (2000), which implements an algorithm by Lanczos (1950), and confirmed that we get practically the same solution as one obtained with BFGS algorithm. Lanczos (1950) algorithm is a commonly used SVD technique applied in case of large sparse matrix or a linear operator, when it is impractical to directly make SVD of A. A truncated SVD of A is given by expression $A \approx U\Sigma V^T$, where Σ is diagonal matrix of n singular values, while U and V are matrices of left and right singular vectors. Variable substitutions

$$z = V^T s, \quad d = U^T b, \tag{4}$$

transforms z into a space of singular vectors s and reduces Eq. (3) to $(\Sigma^T \Sigma + I) \cdot s = \Sigma^T d$, resulting in a solution

$$s = \Sigma^T d/(\Sigma^T \Sigma + I), \tag{5}$$

which is evaluated directly, as Σ is diagonal. In case of having only n largest singular values, the elements of solution s are given by $s_i = \lambda_i d_i/(\lambda_i^2 + 1)$, for all $i \leq n$. Once the solution (5) is found, it is taken back to the space of dimensional fluxes z by applying variable substitutions (4). For fluxes, we have $x = L \cdot z, z = V^T s, d = U^T b$, thus solution is provided by

$$x = LV \cdot \frac{\Sigma^T}{(\Sigma^T\Sigma+I)} \cdot U^T b. \tag{6}$$

Another variant of SVD approach may be more memory efficient in the case of very large dimension of a flux vector, then applying SVD to AA^T instead of A^TA can save some memory as in a representer method (Bennett, 1992). It gives the same solution as SVD of A^TA using less intermediate memory storage when the dimension of the observation vector y is lower compared to that of the flux vector x.

The forward and adjoint mode simulations with transport model needed to implement iterative optimization are composed of several steps:

1. Running the Lagrangian model FLEXPART to produce source-receptor sensitivity matrices. For each observation event, a backward transport simulation with FLEXPART model is implemented, to produce surface flux footprints at a $0.1° \times 0.1°$ latitude-longitude resolution and the 3-D concentration field footprint, taken at the end of the backward simulation run (ending at the coupling time of 00:00 GMT). The coupling time is set to be within 2 to 3 days before observation event. The surface flux sensitivity data are recorded in the unit of ppm(gCm^{-2}day^{-1})$^{-1}$. The flux footprints are saved at daily or hourly timestep, depending on available surface fluxes.

2. Running the coupled transport model forward, which includes:

   a. Running the 3-D Eulerian model NIES-TM from the 3-D initial concentration field, with the prescribed surface fluxes. Sampling the 3-D field at model coupling times for each observation according to 3-D concentration field footprints, calculated at the first step by FLEXPART. NIES-TM reads the same $0.1°$ fluxes as Lagrangian transport model, and remaps them onto its $2.5° \times 2.5°$ grid, before including in the simulation. For each observation event, the fluxes used in Eulerian and Lagrangian components are separated by coupling time, so that there is no double counting of fluxes for same date in the coupled model simulation.

   b. Use two-dimensional (2-D) surface flux footprints prepared with Lagrangian model to calculate the surface flux contribution to the simulated concentrations for the last 3 days.

   c. Combining the concentration contributions produced by Eulerian (a) and Lagrangian (b) component to give total simulated concentration.

3. In the inverse modelling, the transport model is run in three modes:

   a. The forward model is first run with prescribed prior fluxes, starting from the 3-D initial CO$_2$ concentration field, to calculate differences between the observation and the model simulation (residual misfit).

b. at the inverse modelling/optimization step, only flux corrections are propagated in forward model runs, which are optimized to fit the observation-model misfit. The prescribed prior fluxes are not used (switched off) at this step. The model starts from a zero 3-D initial concentration field and runs forward with flux corrections updated by the optimization algorithm at every iteration, to produce simulated concentrations. Corrections to the 3-D initial concentration field are not estimated, and not included into the control vector. Instead, the model is given three months of spin-up period before the target flux estimation period to adjust simulated concentration to observations.

c. in the adjoint mode, the adjoint mode atmospheric transport is simulated backward in time starting from the vector of residuals to produce a gradient of the cost function (defined as eq. (1)) with respect to the surface fluxes. Given the gradient, the optimization algorithm provides the new flux corrections field. For convenience, the transport model and its adjoint are implemented as callable procedures suitable for direct communication mode.

Steps 1 is carried out the same way as in other versions of the coupled transport model (Zhuravlev et al., 2013; Shirai et al., 2017). At steps 2 and 3 the procedure of running the forward and adjoint model is organised differently. At the beginning of the transport model runs, all the data prepared by the Lagrangian model are stored in computer memory, in order to save the time for reading and re-sorting the data at each iteration. The fraction of CPU time spent on running the Eulerian component of the coupled transport model is 82%, on the Lagrangian component 1%, and on covariance 17%.

To create the initial concentration field, we used a 3-D snapshot of CO_2 concentration for the same day from a simulation of previous year, which are already optimised (usually Oct 1st, or Jan 1st)), or, when such simulation is not available, take snapshot from available year and correct it globally for the difference between years using the NOAA monthly mean data for South Pole as representative for the global mean concentration. When the optimised fields are not available, the output of multiyear spin-up simulation is used, with same adjustment to South Pole observations.

4.2   Implementation of covariance matrices *L* and *B*.

We optimized surface flux fields separately for two sets of fluxes in every grid globally, for land and ocean, following the approaches done by Meirink et al. (2008) and Basu et al. (2013), who suggested optimizing for global surface flux fields separately for each optimized flux category. Separating the total flux into independent flux categories, each with its own flux uncertainty pattern, results in using homogenous spatial covariance matrices, significantly simplifying the coding of the matrix *B*. The matrix *B* can be given as a product of a diagonal matrix of flux uncertainties and a matrix with 1.0 as

diagonal elements, while non-diagonal elements are exponentially declining with squared distance between grid points (Meirink et al., 2008). In practice, an extra scaling of the uncertainty is needed for balancing the constraint on fluxes with the data uncertainty, which also impacts the regional flux uncertainties. Several empirical methods are in use, where tuning parameters are horizontal scale (Meirink et al., 2008) and uncertainty multiplier (Chevallier et al., 2005; Rodenbeck, 2005).

5   In our B matrix design, we follow Meirink et al. (2008) in representing B matrix as multiple of non-dimensional covariance matrix C and diagonal matrix of flux uncertainty D as $B = D^T \cdot C \cdot D$. C matrix is commonly implemented as band matrix with non-diagonal elements declining as $\sim \exp(-x^2/l^2)$ with distance x between the grid cells, as in 2-D spline algorithms (Wahba and Wendelberger, 1980). Applying multiplication by matrix C becomes computationally costly at a high spatial resolution in the cases when the correlation distance l is much larger than the size of the model grid. The

10   correlation distance used here is 500 km for land and ocean, and two weeks in time. The rationale of applying a correlation distance of 500 km in case of regional inversion over continental USA with model grid size of 40 km was discussed by Schuh et al. (2010). In that case, the use of implicit diffusion with directional splitting to approximate the Gaussian shape appears to be computationally more efficient than direct application of Gaussian-shaped smoothing function, as the number of floating-point operations per grid point do not grow with the ratio of correlation distance l to the grid size. The

15   covariance matrix based on diffusion operator is popular in many ocean data assimilation systems, as a convenient way to deal with coastlines (e.g. Derber and Rosati, 1989; Weaver and Courtier, 2001).

The idea of using the solution of diffusion equation in place of multiplying a vector by covariance matrix can be presented briefly in a 1-D case. Consider a discrete problem of multiplying a vector representing a function $g(\lambda)$ on a grid with spacing $\Delta\lambda$ by a symmetric matrix which has diagonal elements equal to one, and non-diagonal ones declining as

20   $\exp(-\frac{1}{2}(i\Delta\lambda)^2/d^2)$ with distance of i points from the diagonal, where d is covariance length. Its continuous analogue is an application of a Gaussian-shaped smoother in the form $G(\lambda, \lambda') = \exp(-\frac{1}{2}(\lambda - \lambda')^2/d^2)$ to a function $g(\lambda)$ as:

$$\tilde{g}(\lambda) = \int_{-l}^{l} \exp\left(-\frac{1}{2}(\lambda - \lambda')^2/d^2\right) g(\lambda')\, d\lambda', \tag{7}$$

where smoothing window size l should be several times larger than d. The expression in Eq. (7) looks exactly like a solution of a one-dimensional diffusion equation

25   $$\frac{\partial g}{\partial t} - D\frac{\partial^2 g}{\partial \lambda^2} = 0, \tag{8}$$

where D is a diffusivity. The solution of Eq. (8) is given by $\acute{g}(\lambda) = \frac{1}{\sqrt{2\pi p^2}} \int_{-l}^{l} \exp\left(-\frac{1}{2}(\lambda - \lambda')^2/p^2\right) g(\lambda')\, d\lambda'$, where $p^2 = 2D\Delta t$, $g(\lambda)$ is initial distribution, and Δt is the time step (Crank, 1975). Based on this equivalence, instead of multiplying a vector by covariance matrix, we solve a discrete form of Eq. (8) by backward-in-time, central-in-space implicit method.

Applying diffusion operator for the covariance matrix helps achieving the spatial homogeneity between polar and equatorial regions, as diffusion produces theoretically uniform effect on flux field regardless of the polar singularity. The diffusion operator works as a low-pass filter, selectively suppressing all the wavelengths shorter than the covariance length scale. As we need to construct the covariance matrix B in the form $B = L \cdot L^T$, we choose to construct L first and then derive its transpose L^T. The factorization of L is given by $L = u_F \cdot (L_{xy} \otimes L_t) \cdot m$, where L_t is the one-dimensional covariance matrix for time dimension, $\otimes$ is a Kronecker product. We approximate the two-dimensional covariance L_{xy} by splitting it into two dimensions, latitude and longitude, as in Chua and Bennett, (2001), and apply several iterations of this process. The horizontal covariance L_{xy} is implemented in $N = 3$ iterations of one-dimensional diffusion so that $L_{xy} = (L_x \otimes L_y)^N$, where L_x and L_y are covariance operators for longitude and latitude directions respectively, while u_F is a diagonal matrix of flux uncertainty for each grid cell and each flux category (land and ocean), and m is a diagonal matrix of map factor which is introduced to scale contributions to the cost function by model grid area, with diagonal elements given by $m = \cos^{-1/2} \theta$ (where θ is latitude).

This design of covariance operator helps preserving high-resolution structure of the resultant flux corrections, given by $x = L \cdot z = u_F \cdot (L_{xy} \otimes L_t) \cdot m \cdot z$, as it can be factored into a multiple of uncertainty u_F and scaling factor $S = (L_{xy} \otimes L_t) \cdot m \cdot z$ as $x = u_F \cdot S$. While the scaling factor S is smoothed with covariance length of 500 km, the original structure of spatial heterogeneity of surface flux uncertainty u_F is still present at original high-resolution in the optimised flux corrections x.

The adjoint operators L_x^T, L_y^T are derived by applying the adjoint code compiler Tapenade (Hascoet and Pascual, 2013) to the Fortran code of modules approximating operators L_x and L_y by implicit diffusion. L_t and its transpose L_t^T are of lower dimension and are designed as in Meirink et al. (2008) by deriving a square root of the Gaussian-shaped time covariance matrix with direct SVD (Press et al., 1992).

The important merit of the algorithm is that it makes minimal use of computer memory, avoiding allocation of the memory space larger than several times the dimension of observation and flux vectors, making it suitable for ingesting large amount of surface and space-based observations. It should be mentioned that the computer memory demand for accommodating surface flux sensitivity matrices for massive space-based observations can become a limiting factor as discussed by Miller et al. (2020).

4.3 Inversion setup

Combination of coupled transport model NIES-TM-FLEXPART (as described in Section 2) with variational optimization algorithm (Sections 4.1-4.2) constitutes the inverse modeling system NIES-TM-FLEXPART-VAR (NTFVAR). We test the inversion algorithm presented in previous sections on a problem of finding a best fit to CO_2 observations provide by ObsPack dataset by optimizing corrections to land and ocean fluxes. By the design of our inverse modeling system, we produce smoothed fields of scaling factors that are multiplied by fine resolution flux uncertainty fields to give flux corrections. We derive the surface CO_2 flux corrections at $0.1°$ resolution and half-month time step. Our purpose is to demonstrate that we can optimize fluxes to improve fit to the observations using iterative optimization procedure, based on high-resolution coupled transport model and its adjoint. Our report is limited to technical development towards achieving capability of estimating anthropogenic CO_2 emissions based on atmospheric observations, and we do not elaborate on the impact of improvement in simulating the tracer transport at high resolution on the quality of the optimized natural fluxes, which requires additional study. The flux optimization is applied in a short time-window of 18 months, for each optimized year, and simulation starts on October 1st, three months ahead of the target year. Three-months spin-up period is given to let inversion adjust the modeled concentration to the observations, so that the balance is achieved between fluxes, concentrations and concentration trends. The simulation is continued until reaching the limit of 45 cost function gradient calls, by that time M1QN3 procedure by Gilbert and Lamarechal (1989) is able to complete 30 iterations. Figure A3 in Appendix presents the cost function reduction in case of optimizing fluxes for 2011 and completing 61 gradient calls. The cost function reduction declines nearly exponentially, by almost 3 times for each 10 gradient calls completed. Relative improvement between 41 and 61 gradient calls is 1.5% of the total reduction from the first to the 61 gradient calls. We optimize fluxes for three years from 2010 to 2012, and analyze simulated concentration fit at the observation sites. The average root mean squared misfits (RMSE) between optimized concentration and observations are compared between forward simulation with prior fluxes and optimized simulation, while for evaluation, we use statistics of optimized simulations by the operational CarbonTracker inverse modeling system (ObsPack_co2_1_CARBONTRACKER_CT2017_2018-05-02; Peters et al., 2007).

5   Results and discussion.

5.1 Analysis of the posterior model fit to the observations

We compared the results of forward simulation with prior and optimized fluxes with the processed observations for ground observation sites, as shown in Table A1, and for airborne vertical profiles, used for independent validation (Table A2). Figure 2 shows the observations with forward (prior) and optimized simulations at Barrow (BRW), Jungfraujoch (JFJ), Wisconsin (LEF), Pallas (PAL), Yonagunijima (YON), and Syowa (SYO). Optimization leads to improved seasonal

variation of the simulated concentration, including phase and amplitude at most sites. At SYO we find synoptic scale variations with amplitude in the order of few tenths of a ppm that were to a large extent captured by the model. Plots for BRW and JFJ show the ability of the inversion to correct the seasonal cycle, while the difference between model and observations in the southern hemisphere (SYO) is contributed by interannual variations of the carbon cycle. The model-

5   observation mismatch (RMSE) for surface sites included in the ObsPack is presented in Figure 3 for forward and optimized simulation and mean bias for optimized data. The model was able to reduce the model to observation mismatch for most background sites, where the seasonal cycle is affected mostly by natural terrestrial and oceanic fluxes, while average reduction of the mismatch from forward to optimized simulation is 14%, defined as mean ratio of optimized mismatch to forward mismatch taken for each site. The reason for relatively small reduction is the addition of climatological flux

10   corrections to the prior, estimated by inverse modeling of two years of data, 2009 and 2010. As a result, the inversion starts from the initial flux distributions already adjusted to fit the seasonal cycle of observed concentration. The correction for difference in global concentration trend between years is not made, thus there are visible differences between prior and optimized simulations in southern hemispheric background sites. At most of the Antarctic sites, the mean posterior (after optimization) mismatch (reported as RMSE) is at the level of 0.2 ppm. Over the land, closer to anthropogenic sources,

15   there is less relative reduction of mismatch on average at annual mean scale. One of the reasons for seeing little improvement is keeping fossil CO_2 emissions fixed and optimizing only the natural fluxes (while the strong signal from fossil emission is not affected by flux corrections). Another possible contributor to the large mismatch over land is neglecting the diurnal cycle under assumption of using only observations at well mixed condition, and also the limited ability of the low-resolution reanalysis dataset to capture frontal processes in extratropical continental atmosphere, as

20   discussed by Parazzoo et al. (2011). The mean mismatch is reduced from 2.60 ppm to 2.42 ppm by flux optimization, while the mean mismatch to uncertainty ratio decreases after optimization by 19% from 0.94 to 0.78. The mean correlation between modelled and observed data improves from r^2 =0.43 (r^2 - coefficient of determination) for simulation driven by prior fluxes to r^2 =0.59 for optimized simulation. To remove the effect of interannual CO_2 growth on CO_2 variability the mean growth trend was subtracted from data before estimating the r^2.

25   Figure 3 also shows, for comparison, the statistics of the average misfit for optimized simulation by CarbonTracker, for the same period and same monitoring stations. The comparison is useful for understanding the strength and weaknesses of the inversion system presented here. Over the background monitoring sites, the high-resolution model does not show advantage over CarbonTracker in terms of the fit between optimized model simulation and observations, which may indicate a better performance by the Eulerian model TM5 used in CarbonTracker. On the other hand, several sites where

30   the high-resolution model shows better fits to observations over CarbonTracker are located inland or near the coast, closer to anthropogenic and biogenic sources. Lower misfit is achieved by high-resolution model at Key Biscaine (KEY), Baring

Head (BHD), Marianna island (GMI) and Cape Kumukahi (KUM), among others, which can be attributed to coastal/island locations, while there is little or no advantage at mountain sites like Mauna Loa (MLO) or Jungfraujoch (JFJ). This result may be influenced by differences in the model physics between NIES-TM-FLEXPART and TM5 in the lower troposphere, near the top of the boundary layer and in shallow cumuli. The mismatch (RMSE) between our optimized model and observations for the 102 sites used in the inversion is only 4% lower on average than that by CarbonTracker. It is not yet clear if there is a systematic advantage of one or another system in any particular site category, other than for coastal/island sites mentioned above. For average misfit comparison, all data, both assimilated and not assimilated, are included for sites shown in Figure 3. The results for CGO were not counted, due to the use of different datasets, as our system used only NOAA flask data, which underwent background selection (by wind direction) at the time of sampling.

For independent validation, a comparison of the unoptimized and optimized simulation to the vertical profile data is shown in Figure 4. For each vertical profile site, the observations were grouped according to altitude range, at 1 km steps. Altitude code (e.g. 005, 015, 025, 035, …) to be added to site the identifier is constructed as altitude of midlevel multiplied by 10. The observations at PFA (Poker Fat Alaska) between surface and 1 km are grouped as PFA005 (mid altitude 0.5 km), while those in 5 to 6 km range are designated as PFA055 (mid altitude 5.5 km). As for optimized surface data in Figure 3, we show RMSE for forward simulation with prior fluxes, optimized simulation and CarbonTracker, and mean bias for optimized data. CarbonTracker shows better fit at most altitudes except for the lowest 1 km where the results shown by the two systems are similar. Concurrently, mean correlation between modelled and observed data does not improve from prior (r^2 =0.70) to optimized simulation (r^2 =0.63), while mean RMSE declines a little from 1.86 ppm to 1.85 ppm. Comparison to CarbonTracker (CT2017), with mean RMSE of 1.53 ppm, suggests that free tropospheric performance can be improved by implementing more detailed vertical mixing processes in the Lagrangian and Eulerian component models.

5.2 Comparison of prior and posterior fluxes

As mentioned in section 4.2, the flux corrections estimated by the inverse model appear as high-resolution despite using large covariance length, because those are made of the high-resolution data uncertainty multiplied by the smooth fields of scaling factor, estimated separately for each of the optimized flux categories - land biosphere and ocean. Examples of the flux correction and posterior fluxes (excluding fossil emissions) are presented on Figure 5. The flux corrections and fluxes are shown on Figure 5 for one month (Aug 2011) as illustration and are not representative of a seasonal or climatological mean. The sign of the flux correction changes from positive (source) in the eastern side (continental China) to negative (sink) over Russian coast and Japanese islands, while the posterior fluxes show terrestrial sink all over the area. The flux adjustment is driven by the fit to nearby observations made over Korea and Japan.

To illustrate the change of fluxes from prior to posterior estimate by inversion at the scale of large regions, the monthly mean fluxes (excluding fossil emissions) averaged for 3 years 2010-2012 are plotted in Figure 6 for eight selected Transcom regions (as defined by Gurney et al. 2002, see map in Figure A2). The plots include prior, optimized and, for reference, optimized fluxes by CarbonTracker (CT2017). For some regions, the posterior is close to prior, which is often the case when there are too few observations in the region to drive the corrections to prior fluxes. Boreal North America (region 1), Temperate North America (2), and Europe (11) are better constrained by observations, while North Africa (5), South Africa (6), Temperate Asia (8), South-East Asia (9) and Boreal Asia (7) are less constrained. The optimized flux is similar to the prior for Africa (5, 6), South-East Asia (10) and Temperate Asia (8), while there is substantial adjustment for Boreal Asia (7), which seems to be adjusted to fit the observations outside the region. For both boreal regions the prior flux seasonality appears weaker than in both posterior and CarbonTracker, which could indicate a problem with vegetation type mapping in higher resolution version of prior flux model. For regions 1, 6, 7 and 11, the corrected fluxes are closer to CarbonTracker, and for Temperate North America, Temperate Asia and North Africa the amplitude of flux seasonality is estimated to be stronger, which can be caused by stronger vertical/horizontal mixing in transport model as compared to the transport in CarbonTracker. More detailed comparison with other inverse model results and independent estimates (e.g. by Jung et al., 2020) should be made after improving the inversion setup, notably, improving the transport model meteorology, seasonality and diurnal cycle in prior fluxes and seasonality in prior flux uncertainties.

6 Summary and conclusions

A grid-based flux inversion system was developed, which is suitable for inverse estimation of the surface fluxes at biweekly time step and 0.1° spatial resolution. To implement the high-resolution capability, several developments were completed. High-resolution prior fluxes were prepared for three surface flux categories: fossil emissions by ODIAC dataset are based on point source database and nightlights, biomass burning emissions (GFAS) are based on MODIS observations of fire radiative power and biosphere exchange is based on mosaic representation of landcover and process-based VISIT model simulation. High-resolution transport for global set of observations is achieved by combining short-term simulations with high-resolution Lagrangian model FLEXPART with global three-dimensional simulation with medium-resolution Eulerian model NIES-TM. Use of variational optimization with a gradient-based method in the inversion helps avoiding the need to invert large matrices with dimensions dictated by the number of optimized grid fluxes or the number of the observations. Accordingly, the adjoint of the coupled transport model was developed to apply the variational optimization. Computationally efficient implementation of flux error covariance operator is achieved by using implicit diffusion algorithm. Overall, the presented algorithm demonstrates feasibility of high-resolution inverse modeling at global scale,

extending the capabilities achieved by regional high-resolution modeling approaches used for estimating the national greenhouse gas emissions for comparison to the national greenhouse gas inventories. Comparison of the optimized simulation to the observations shows some improvement over lower resolution CarbonTracker model for some continental and coastal observation sites, located closer to anthropogenic emissions and strong biospheric fluxes, but also demonstrates

5 the need for further improvement of the inverse modeling system components. Transport model errors can be reduced by improving transport modeling algorithms in Eulerian and Lagrangian model and using combination of recent higher resolution reanalysis data with high-resolution wind data simulations by regional models in the regions of interest. Inverse modeling algorithm can be improved by tuning the uncertainty scaling, and spatial and temporal covariance distances. Prior fluxes can be improved by developing high-resolution diurnally varying biospheric fluxes, developing a more detailed

10 fossil emission inventory, and developing updates to biomass burning and oceanic fluxes.

Code and data availability.

The inverse model and forward transport model code can be made available to research collaborators. Observed CO_2 concentrations ObsPack dataset is available from NOAA/ESRL (https://www.esrl.noaa.gov/gmd/ccgg/obspack/), ODIAC fossil fuel emissions - from CGER/NIES database (http://db.cger.nies.go.jp/dataset/ODIAC/).

15 **Author contributions.**

SM developed the inverse and transport model algorithms and model codes, ran the model, analysed the results and wrote the manuscript. TO developed the anthropogenic emission inventory, MS developed biospheric flux dataset, JK provided the biomass burning emission fluxes, VV prepared the oceanic CO_2 fluxes. RJ contributed to model testing and data preparation, DB contributed to the development of the NIES transport model, coupled model and coupled adjoint, RZ and

20 AG developed the Lagrangian response simulation system based on FLEXPART model. AA, LC, ED, LH, TM, TN, MR, RL, CS, DR contributed the observational data. All the authors contributed to the development of the manuscript.

Competing interests.

The authors declare no competing interests.

Acknowledgements

The authors acknowledge the use of computing resources at the National Institute for Environmental Studies (NIES) super-computer facility and support from the GOSAT project, project leaders Tatsuya Yokota and Tsuneo Matsunaga, the Ministry of the Environment (MOE) Japan, MRV grant to NIES, grants by the Ministry of Education, Culture, Sports, Science and Technology (MEXT) of Japan to GRENE and ArCS projects. The model development benefitted from fruitful discussions with Frederic Chevallier, David Baker, Peter Rayner, Aki Tsuruta, Fenjuan Wang, Prabir Patra, John Miller, Misa Ishizawa, Tomoko Shirai and the members of the TRANSCOM project. Lorna Nayagam provided her technical assistance to our model testing and dataset developments. Authors appreciate contribution of NOAA CarbonTracker data provided by Andy Jacobson and colleagues. The ObsPack was compiled and distributed by NOAA/ESRL. The authors are grateful to the ObsPack data contributors at NOAA GMD, the Environment and Climate Change Canada and other institutions worldwide, including Tuula Aalto, Shuji Aoki, Gordon Brailsford, Marc L. Fischer, Grant Forster, Angel J. Gomez-Pelaez, Juha Hatakka, Arjan Hensen, Casper Labuschagne, Ralph Keeling, Paul Krummel, Markus Leuenberger, Andrew Manning, Kathryn McKain, Frank Meinhardt, Harro Meijer, Shinji Morimoto, Jaroslaw Necki, Paul Steele, Britton Stephens, Atsushi Takizawa, Pieter Tans, Kirk Thoning and their colleagues.

Appendix

Table A1. List of the observation site included in the ObsPack dataset

Site ID	Lat	Lon.	Site name	Lab name	Sampling	Reference
ALT	82.45	-62.51	Alert	EC	insitu	Worthy et al. 2003
ALT	82.45	-62.51	Alert	NOAA	flask	Conway et al. 1994
AMS	-37.8	77.54	Amsterdam Island	LSCE	insitu	Gaudry et al. 1991
AMT	45.03	-68.68	Argyle	NOAA	insitu	Andrews et al. 2014
ARA	-23.86	148.47	Arcturus	CSIRO	flask	Francey et al. 2003
ASC	-7.97	-14.40	Ascension Island	NOAA	flask	Conway et al. 1994
ASK	23.26	5.63	Assekrem	NOAA	flask	Conway et al. 1994
AZR	38.77	-27.38	Terceira Island	NOAA	flask	Conway et al. 1994
BAO	40.05	-105.00	Boulder Atmospheric Observatory	NOAA	insitu	Andrews et al. 2014
BCK	-116.1	62.80	Bechoko	EC	insitu	Worthy et al. 2003
BHD	-41.41	174.87	Baring Head Station	NOAA	flask	Conway et al. 1994

BHD	-41.41	174.87	Baring Head Station	NIWA	insitu	Brailsford et al. 2012
BMW	32.27	-64.88	Tudor Hill	NOAA	flask	Conway et al. 1994
BRA	51.2	-104.7	Bratt's Lake Saskatchewan	EC	insitu	Worthy et al. 2003
BRW	71.32	-156.61	Barrow	NOAA	flask	Conway et al. 1994
BRW	71.32	-156.61	Barrow	NOAA	insitu	Peterson et al. 1986
CBA	55.21	-162.72	Cold Bay	NOAA	flask	Conway et al. 1994
CES	51.97	4.93	Cesar	ECN	insitu	Vermeulen et al. 2011
CGO	-40.68	144.69	Cape Grim	NOAA	flask	Conway et al. 1994
CHL	58.75	-94.07	Churchill	EC	insitu	Worthy et al. 2003
CHR	1.70	-157.15	Christmas Island	NOAA	flask	Conway et al. 1994
CIB	41.81	-4.93	Centro de Investigacion de la Baja Atmosfera	NOAA	flask	Conway et al. 1994
CPT	-34.35	18.49	Cape Point	NOAA	flask	Conway et al. 1994
CPT	-34.35	18.49	Cape Point	SAWS	insitu	Brunke et al. 2004
CRI	15.08	73.83	Cape Rama	CSIRO	flask	Francey et al. 2003
CRZ	-46.43	51.85	Crozet Island	NOAA	flask	Conway et al. 1994
CYA	-66.28	110.52	Casey	CSIRO	flask	Francey et al. 2003
DRP	-59.12	-63.63	Drake Passage	NOAA	ship flask	Conway et al. 1994
EGB	44.23	-79.78	Egbert	EC	insitu	Worthy et al. 2003
EIC	-27.15	-109.45	Easter Island	NOAA	flask	Conway et al. 1994
ESP	49.38	-126.54	Estevan Point	EC	insitu	Worthy et al. 2003
EST	51.66	-110.21	Esther	EC	insitu	Worthy et al. 2003
ETL	54.35	-104.98	East Trout Lake	EC	insitu	Worthy et al. 2003
FSD	49.88	-81.57	Fraserdale	EC	insitu	Worthy et al. 2003
GMI	13.39	144.66	Mariana Islands	NOAA	flask	Conway et al. 1994
GPA	-12.25	131.04	Gunn Point	CSIRO	flask	Francey et al. 2003
HBA	-75.61	-26.21	Halley Station	NOAA	flask	Conway et al. 1994
HDP	40.56	-111.65	Hidden Peak (Snowbird)	NCAR	insitu	Stephens et al. 2011
HPB	47.80	11.02	Hohenpeissenberg	NOAA	flask	Conway et al. 1994
HUN	46.95	16.65	Hegyhatsal	HMS	insitu	Haszpra et al. 2001

HUN	46.95	16.65	Hegyhatsal	NOAA	flask	Conway et al. 1994
INX	-86.02	39.79	INFLUX (Indianapolis Flux Experiment)	NOAA	flask	Conway et al. 1994
IZO	28.31	-16.50	Izana	NOAA	flask	Conway et al. 1994
IZO	28.31	-16.50	Izana	AEMET	insitu	Gomez-Pelaez et al. 2011
JFJ	46.55	7.99	Jungfraujoch	KUP	insitu	Uglietti et al. 2011
KAS	49.23	19.98	Kasprowy Wierch	AGH	insitu	Necki et al. 2003
KEY	25.66	-80.16	Key Biscayne	NOAA	flask	Conway et al. 1994
KUM	19.52	-154.82	Cape Kumukahi	NOAA	flask	Conway et al. 1994
LEF	45.95	-90.27	Park Falls	NOAA	insitu	Andrews et al. 2014
LJO	32.87	-117.26	La Jolla	SIO	flask	Keeling et al. 2005
LLB	54.95	-112.45	Lac La Biche	EC	insitu	Worthy et al. 2003
LLB	54.95	-112.45	Lac La Biche	NOAA	flask	Conway et al. 1994
LMP	35.52	12.62	Lampedusa	NOAA	flask	Conway et al. 1994
LUT	53.4	6.35	Lutjewad	RUG	insitu	van der Laan et al. 2009
MAA	-67.62	62.87	Mawson Station	CSIRO	flask	Francey et al. 2003
MEX	18.98	-97.31	High Altitude Global Climate Observation Center	NOAA	flask	Conway et al. 1994
MHD	53.33	-9.9	Mace Head	NOAA	flask	Conway et al. 1994
MHD	53.33	-9.9	Mace Head	LSCE	insitu	Ramonet et al. 2010
MID	28.21	-177.38	Sand Island	NOAA	flask	Conway et al. 1994
MLO	19.54	-155.58	Mauna Loa	NOAA	flask	Conway et al. 1994
MLO	19.54	-155.58	Mauna Loa	NOAA	insitu	Thoning et al. 1989
MNM	24.28	153.98	Minamitorishima	JMA	insitu	Tsutsumi et al. 2005
MQA	-54.48	158.97	Macquarie Island	CSIRO	flask	Francey et al. 2003
NAT	-5.51	-35.26	Farol De Mae Luiza Lighthouse	NOAA	flask	Conway et al. 1994
NMB	-23.58	15.03	Gobabeb	NOAA	flask	Conway et al. 1994
NWR	40.05	-105.59	Niwot Ridge	NOAA	flask	Conway et al. 1994

NWR	40.05	-105.59	Niwot Ridge	NCAR	insitu	Stephens et al. 2011
OTA	-38.52	142.82	Otway	CSIRO	flask	Francey et al. 2003
OXK	50.03	11.81	Ochsenkopf	NOAA	flask	Conway et al. 1994
PAL	67.97	24.12	Pallas-Sammaltunturi	NOAA	flask	Conway et al. 1994
PAL	67.97	24.12	Pallas-Sammaltunturi	FMI	insitu	Hatakka et al. 2003
POC			Pacific Ocean Cruise	NOAA	flask	Conway et al. 1994
PSA	-64.92	-64	Palmer Station	NOAA	flask	Conway et al. 1994
RPB	13.16	-59.43	Ragged Point	NOAA	flask	Conway et al. 1994
RYO	39.03	141.82	Ryori	JMA	insitu	Tsutsumi et al. 2005
SCT	33.41	-81.83	Beech Island	NOAA	insitu	Andrews et al. 2014
SEY	-4.68	55.53	Mahe Island	NOAA	flask	Conway et al. 1994
SGP	36.8	-97.5	Southern Great Plains	NOAA	flask	Conway et al. 1994
SHM	52.72	174.1	Shemya Island	NOAA	flask	Conway et al. 1994
SMO	-14.25	-170.56	Tutuila	NOAA	flask	Conway et al. 1994
SMO	-14.25	-170.56	Tutuila	NOAA	insitu	Halter et al. 1988
SNP	38.62	-78.35	Shenandoah National Park	NOAA	insitu	Andrews et al. 2014
SPL	40.45	-106.73	Storm Peak Laboratory (Desert Research Institute)	NCAR	insitu	Stephens et al. 2011
SPO	-89.98	-24.8	South Pole	NOAA	flask	Conway et al. 1994
SPO	-89.98	-24.8	South Pole	NOAA	insitu	Gillette et al. 1987
STR	37.76	-122.45	Sutro Tower	NOAA	flask	Andrews et al. 2014
SUM	72.6	-38.42	Summit	NOAA	flask	Conway et al. 1994
SYO	-69.01	39.59	Syowa Station	NOAA	insitu	Morimoto et al. 2003
TAP	36.73	126.13	Tae-ahn Peninsula	NOAA	flask	Conway et al. 1994
THD	41.05	-124.15	Trinidad Head	NOAA	flask	Conway et al. 1994
USH	-54.85	-68.31	Ushuaia	NOAA	flask	Conway et al. 1994
UTA	39.9	-113.72	Wendover	NOAA	flask	Conway et al. 1994
UUM	44.45	111.1	Ulaan Uul	NOAA	flask	Conway et al. 1994
WAO	52.95	1.12	Weybourne	UEA	insitu	Forster and Bandy, 2006

WBI	41.73	-91.35	West Branch	NOAA	insitu	Andrews et al. 2014
WGC	38.27	-121.49	Walnut Grove	NOAA	insitu	Andrews et al. 2014
WIS	30.86	34.78	Weizmann Institute of Science	NOAA	flask	Conway et al. 1994
WKT	31.32	-97.33	Moody	NOAA	insitu	Andrews et al. 2014
WLG	36.29	100.9	Mt. Waliguan	NOAA	flask	Conway et al. 1994
WSA	43.93	-60.02	Sable Island	EC	insitu	Worthy et al. 2003
YON	24.47	123.02	Yonagunijima	JMA	insitu	Tsutsumi et al. 2005
ZEP	78.91	11.89	Ny-Alesund	NOAA	flask	Conway et al. 1994

Table A2. Validation sites. Aircraft data collected by NOAA/ESRL (Sweeney et al., 2015) and NIES (Machida et al., 2008)

Site ID	Lat.	Lon.	Site/project name	Territory	Lab name
ACG	68	-165	Alaska Coast Guard	Alaska	NOAA
CAR	41	-104	Briggsdale	Colorado	NOAA
CMA	39	-74	Offshore Cape May	New Jersey	NOAA
CON			CONTRAIL	West Pacific	NIES
DND	47	-99	Dahlen	North Dakota	NOAA
ESP	49	-127	Estevan Point	British Columbia	NOAA
ETL	54	-105	East Trout Lake	Saskatchewan	NOAA
INX	40	-86	Indianapolis Flux Experiment	Indianapolis	NOAA
LEF	46	-90	Park Falls	Wisconsin	NOAA
HIL	40	-88	Homer	Illinois	NOAA
NHA	43	-71	Offshore Portsmouth	New Hampshire	NOAA
PFA	65	-148	Poker Flat	Alaska	NOAA
RTA	-21	-160	Rarotonga	Rarotonga	NOAA
SCA	33	-79	Offshore Charleston	South Carolina	NOAA
SGP	37	-98	Southern Great Plains	Oklahoma	NOAA
TGC	28	-97	Offshore Corpus Christi	Texas	NOAA

References

Agustí-Panareda, A., Diamantakis, M., Massart, S., Chevallier, F., Muñoz-Sabater, J., Barré, J., Curcoll, R., Engelen, R., Langerock, B., Law, R. M., Loh, Z., Morguí, J. A., Parrington, M., Peuch, V. H., Ramonet, M., Roehl, C., Vermeulen, A.

5   T., Warneke, T., and Wunch, D.: Modelling CO_2 weather – why horizontal resolution matters, Atmos. Chem. Phys., 19, 7347-7376, 10.5194/acp-19-7347-2019, 2019.

Andres, R., Gregg, J., Losey, L., Marland, G., and Boden, T.: Monthly, global emissions of carbon dioxide from fossil fuel consumption, Tellus Series B-Chemical and Physical Meteorology, 63, 309-327, 10.1111/j.1600-0889.2011.00530.x, 2011.

10   Andrews, A. E., Kofler, J. D., Trudeau, M. E., Williams, J. C., Neff, D. H., Masarie, K. A., Chao, D. Y., Kitzis, D. R., Novelli, P. C., Zhao, C. L., Dlugokencky, E. J., Lang, P. M., Crotwell, M. J., Fischer, M. L., Parker, M. J., Lee, J. T., Baumann, D. D., Desai, A. R., Stanier, C. O., De Wekker, S. F. J., Wolfe, D. E., Munger, J. W., and Tans, P. P.: CO2, CO, and CH4 measurements from tall towers in the NOAA Earth System Research Laboratory's Global Greenhouse Gas Reference Network: instrumentation, uncertainty analysis, and recommendations for future high-accuracy greenhouse gas

15   monitoring efforts, Atmos. Meas. Tech., 7, 647-687, 10.5194/amt-7-647-2014, 2014.

Baker, D., Doney, S., and Schimel, D.: Variational data assimilation for atmospheric CO_2, Tellus Series B-Chemical and Physical Meteorology, 58, 359-365, 10.1111/j.1600-0889.2006.00218.x, 2006.

Basu, S., Guerlet, S., Butz, A., Houweling, S., Hasekamp, O., Aben, I., Krummel, P., Steele, P., Langenfelds, R., Torn, M., Biraud, S., Stephens, B., Andrews, A., and Worthy, D.: Global CO_2 fluxes estimated from GOSAT retrievals of total

20   column CO_2, Atmospheric Chemistry and Physics, 13, 8695-8717, 10.5194/acp-13-8695-2013, 2013.

Belikov, D. A., Maksyutov, S., Sherlock, V., Aoki, S., Deutscher, N. M., Dohe, S., Griffith, D., Kyro, E., Morino, I., Nakazawa, T., Notholt, J., Rettinger, M., Schneider, M., Sussmann, R., Toon, G. C., Wennberg, P. O., and Wunch, D.: Simulations of column-averaged CO_2 and CH_4 using the NIES TM with a hybrid sigma-isentropic (sigma-theta) vertical coordinate, Atmospheric Chemistry and Physics, 13, 1713-1732, 10.5194/acp-13-1713-2013, 2013.

25   Belikov, D. A., Maksyutov, S., Yaremchuk, A., Ganshin, A., Kaminski, T., Blessing, S., Sasakawa, M., Gomez-Pelaez, A. J., and Starchenko, A.: Adjoint of the global Eulerian-Lagrangian coupled atmospheric transport model (A-GELCA v1.0): development and validation, Geoscientific Model Development, 9, 749-764, 10.5194/gmd-9-749-2016, 2016.

Bennett, A. F.: Inverse Methods in Physical Oceanography, Cambridge Monographs on Mechanics, Cambridge University Press, Cambridge, 1992.

Brailsford, G., Stephens, B., Gomez, A., Riedel, K., Fletcher, S., Nichol, S., and Manning, M.: Long-term continuous atmospheric CO_2 measurements at Baring Head, New Zealand, Atmospheric Measurement Techniques, 5, 3109-3117, 10.5194/amt-5-3109-2012, 2012.

Broyden, C.: A New Double-Rank Minimisation Algorithm. Preliminary Report, Notices of the American Mathematical Society, 16, 670-670, 1969.

Brunke, E., Labuschagne, C., Parker, B., Scheel, H., and Whittlestone, S.: Baseline air mass selection at Cape Point, South Africa: application of Rn-222 and other filter criteria to CO_2, Atmospheric Environment, 38, 5693-5702, 10.1016/j.atmosenv.2004.04.024, 2004.

Chevallier, F., Fisher, M., Peylin, P., Serrar, S., Bousquet, P., Breon, F., Chedin, A., and Ciais, P.: Inferring CO_2 sources and sinks from satellite observations: Method and application to TOVS data, Journal of Geophysical Research-Atmospheres, 110, 10.1029/2005JD006390, 2005.

Chua, B., and Bennett, A.: An inverse ocean modeling system, Ocean Modelling, 3, 137-165, 10.1016/S1463-5003(01)00006-3, 2001.

Conway, T. J., Tans, P. P., Waterman, L. S., Thoning, K. W., Kitzis, D. R., Masarie, K. A., and Zhang, N.: Evidence for interannual variability of the carbon cycle from the National Oceanic and Atmospheric Administration/Climate Monitoring and Diagnostics Laboratory Global Air Sampling Network, Journal of Geophysical Research: Atmospheres, 99, 22831-22855, 10.1029/94jd01951, 1994.

Cooperative Global Atmospheric Data Integration Project: Multi-laboratory compilation of atmospheric carbon dioxide data for the period 1957-2015; ObsPack_co2_1_GLOBALVIEWplus_v2.1_2016-09-02. NOAA Earth System Research Laboratory, Global Monitoring Division, 2016.

Crank, J.: The Mathematics of Diffusion, 2nd edition, Oxford Univ. Press, 414, 1975

Denning, A. S., Randall, D. A., Collatz, G. J., and Sellers, P. J.: Simulations of terrestrial carbon metabolism and atmospheric CO_2 in a general circulation model, Tellus B: Chemical and Physical Meteorology, 48, 543-567, 10.3402/tellusb.v48i4.15931, 1996.

Derber, J., and Rosati, A.: A Global Oceanic Data Assimilation System, Journal of Physical Oceanography, 19, 1333-1347, 10.1175/1520-0485(1989)019<1333:AGODAS>2.0.CO;2, 1989.

Elvidge, C., Baugh, K., Dietz, J., Bland, T., Sutton, P., and Kroehl, H.: Radiance calibration of DMSP-OLS low-light imaging data of human settlements, Remote Sensing of Environment, 68, 77-88, 10.1016/S0034-4257(98)00098-4, 1999.

Enting, I. G., and Mansbridge, J. V.: Seasonal sources and sinks of atmospheric CO_2 Direct inversion of filtered data, Tellus B, 41B, 111-126, 10.3402/tellusb.v41i2.15056, 1989.

Enting, I. G.: Inverse Problems in Atmospheric Constituent Transport, Cambridge Atmospheric and Space Science Series, Cambridge University Press, Cambridge, 2002.

Fisher, M., and Courtier, P.: Estimating the covariance matrices of analysis and forecast error in variational data assimilation, ECMWF, Shinfield Park, Reading, 26, 1995.

5   Forster, G., and Bandy, B.: Weybourne Atmospheric Observatory (WAO): surface meteorology and atmospheric chemistry data. NCAS British Atmospheric Data Centre, (accessed 03/10/2020), http://catalogue.ceda.ac.uk/uuid/36517548500e1e4e85c97d99457e268a, 2006

Ganshin, A., Oda, T., Saito, M., Maksyutov, S., Valsala, V., Andres, R. J., Fisher, R. E., Lowry, D., Lukyanov, A., Matsueda, H., Nisbet, E. G., Rigby, M., Sawa, Y., Toumi, R., Tsuboi, K., Varlagin, A., and Zhuravlev, R.: A global coupled

10   Eulerian-Lagrangian model and 1x1 km CO_2 surface flux dataset for high-resolution atmospheric CO_2 transport simulations, Geoscientific Model Development, 5, 231-243, 10.5194/gmd-5-231-2012, 2012.

Gaudry, A., Monfray, P., Polian, G., Bonsang, G., Ardouin, B., Jegou, A., and Lambert, G.: Non-seasonal variations of atmospheric CO_2 concentrations at Amsterdam Island, Tellus B: Chemical and Physical Meteorology, 43, 136-143, 10.3402/tellusb.v43i2.15258, 1991.

15   Giering, R., and Kaminski, T.: Applying TAF to generate efficient derivative code of Fortran 77-95 programs, PAMM, 2, 54-57, 10.1002/pamm.200310014, 2003.

Gilbert, J., and Lemarechal, C.: Some numerical experiments with variable-storage quasi-newton algorithms, Mathematical Programming, 45, 407-435, 10.1007/BF01589113, 1989.

Gillette, D. A., Komhyr, W. D., Waterman, L. S., Steele, L. P., and Gammon, R. H.: The NOAA/GMCC continuous CO_2

20   record at the South Pole, 1975–1982, Journal of Geophysical Research: Atmospheres, 92, 4231-4240, 10.1029/JD092iD04p04231, 1987.

Gurney, K., Law, R., Denning, A., Rayner, P., Baker, D., Bousquet, P., Bruhwiler, L., Chen, Y., Ciais, P., Fan, S., Fung, I., Gloor, M., Heimann, M., Higuchi, K., John, J., Maki, T., Maksyutov, S., Masarie, K., Peylin, P., Prather, M., Pak, B., Randerson, J., Sarmiento, J., Taguchi, S., Takahashi, T., and Yuen, C.: Towards robust regional estimates of CO_2 sources

25   and sinks using atmospheric transport models, Nature, 415, 626-630, 10.1038/415626a, 2002.

Halter, B. C., Harris, J. M., and Conway, T. J.: Component signals in the record of atmospheric carbon dioxide concentration at American Samoa, Journal of Geophysical Research: Atmospheres, 93, 15914-15918, 10.1029/JD093iD12p15914, 1988.

Hascoet, L., and Pascual, V.: The Tapenade Automatic Differentiation Tool: Principles, Model, and Specification, Acm

30   Transactions on Mathematical Software, 39, 10.1145/2450153.2450158, 2013.

Haszpra, L., Barcza, Z., Bakwin, P. S., Berger, B. W., Davis, K. J., and Weidinger, T.: Measuring system for the long-term monitoring of biosphere/atmosphere exchange of carbon dioxide, Journal of Geophysical Research: Atmospheres, 106, 3057-3069, 10.1029/2000jd900600, 2001.

He, W., van der Velde, I. R., Andrews, A. E., Sweeney, C., Miller, J., Tans, P., van der Laan-Luijkx, I. T., Nehrkorn, T.,

5   Mountain, M., Ju, W., Peters, W., and Chen, H.: CTDAS-Lagrange v1.0: a high-resolution data assimilation system for regional carbon dioxide observations, Geosci. Model Dev., 11, 3515-3536, 10.5194/gmd-11-3515-2018, 2018.

Henne, S., Brunner, D., Oney, B., Leuenberger, M., Eugster, W., Bamberger, I., Meinhardt, F., Steinbacher, M., and Emmenegger, L.: Validation of the Swiss methane emission inventory by atmospheric observations and inverse modelling, Atmospheric Chemistry and Physics, 16, 3683-3710, 2016.

10 Ito, A.: Changing ecophysiological processes and carbon budget in East Asian ecosystems under near-future changes in climate: implications for long-term monitoring from a process-based model, Journal of Plant Research, 123, 577-588, 10.1007/s10265-009-0305-x, 2010.

Janardanan, R., Maksyutov, S., Tsuruta, A., Wang, F., Tiwari, Y. K., Valsala, V., Ito, A., Yoshida, Y., Kaiser, J. W., Janssens-Maenhout, G., Arshinov, M., Sasakawa, M., Tohjima, Y., Worthy, D. E. J., Dlugokencky, E. J., Ramonet, M.,

15 Arduini, J., Lavric, J. V., Piacentino, S., Krummel, P. B., Langenfelds, R. L., Mammarella, I., and Matsunaga, T.: Country-Scale Analysis of Methane Emissions with a High-Resolution Inverse Model Using GOSAT and Surface Observations, Remote Sensing, 12, 375, 2020.

Jung, M., Henkel, K., Herold, M., and Churkina, G.: Exploiting synergies of global land cover products for carbon cycle modeling, Remote Sensing of Environment, 101, 534-553, 10.1016/j.rse.2006.01.020, 2006.

20 Jung, M., Schwalm, C., Migliavacca, M., Walther, S., Camps-Valls, G., Koirala, S., Anthoni, P., Besnard, S., Bodesheim, P., Carvalhais, N., Chevallier, F., Gans, F., Goll, D. S., Haverd, V., Köhler, P., Ichii, K., Jain, A. K., Liu, J., Lombardozzi, D., Nabel, J. E. M. S., Nelson, J. A., O'Sullivan, M., Pallandt, M., Papale, D., Peters, W., Pongratz, J., Rödenbeck, C., Sitch, S., Tramontana, G., Walker, A., Weber, U., and Reichstein, M.: Scaling carbon fluxes from eddy covariance sites to globe: synthesis and evaluation of the FLUXCOM approach, Biogeosciences, 17, 1343-1365, 10.5194/bg-17-1343-2020,

25 2020.

Kaiser, J. W., Heil, A., Andreae, M. O., Benedetti, A., Chubarova, N., Jones, L., Morcrette, J. J., Razinger, M., Schultz, M. G., Suttie, M., and van der Werf, G. R.: Biomass burning emissions estimated with a global fire assimilation system based on observed fire radiative power, Biogeosciences, 9, 527-554, 10.5194/bg-9-527-2012, 2012.

Kaminski, T., Rayner, P., Heimann, M., and Enting, I.: On aggregation errors in atmospheric transport inversions, Journal

30 of Geophysical Research-Atmospheres, 106, 4703-4715, 10.1029/2000JD900581, 2001.

Keeling, C. D., Piper, S. C., Bacastow, R. B., Wahlen, M., Whorf, T. P., Heimann, M., and Meijer, H. A.: Atmospheric CO_2 and $^{13}CO_2$ Exchange with the Terrestrial Biosphere and Oceans from 1978 to 2000: Observations and Carbon Cycle Implications, in: A History of Atmospheric CO_2 and Its Effects on Plants, Animals, and Ecosystems, edited by: Baldwin, I. T., Caldwell, M. M., Heldmaier, G., Jackson, R. B., Lange, O. L., Mooney, H. A., Schulze, E. D., Sommer, U., Ehleringer,

5   J. R., Denise Dearing, M., and Cerling, T. E., Springer New York, New York, NY, 83-113, 2005.

Lanczos, C.: An Iteration Method For The Solution Of The Eigenvalue Problem Of Linear Differential And Integral Operators, Journal of Research of the National Bureau of Standards, 45, 255-282, 10.6028/jres.045.026, 1950.

Lauvaux, T., Miles, N., Deng, A., Richardson, S., Cambaliza, M., Davis, K., Gaudet, B., Gurney, K., Huang, J., O'Keefe, D., Song, Y., Karion, A., Oda, T., Patarasuk, R., Razlivanov, I., Sarmiento, D., Shepson, P., Sweeney, C., Turnbull, J., and

10   Wu, K.: High-resolution atmospheric inversion of urban CO_2 emissions during the dormant season of the Indianapolis Flux Experiment (INFLUX), Journal of Geophysical Research-Atmospheres, 121, 5213-5236, 10.1002/2015JD024473, 2016.

Lauvaux, T., Gurney, K. R., Miles, N. L., Davis, K. J., Richardson, S. J., Deng, A., Nathan, B. J., Oda, T., Wang, J. A., Hutyra, L., and Turnbull, J.: Policy-Relevant Assessment of Urban CO_2 Emissions, Environmental Science & Technology, 54, 10237-10245, 10.1021/acs.est.0c00343, 2020.

15   Law, R. M., Peters, W., Roedenbeck, C., Aulagnier, C., Baker, I., Bergmann, D. J., Bousquet, P., Brandt, J., Bruhwiler, L., Cameron-Smith, P. J., Christensen, J. H., Delage, F., Denning, A. S., Fan, S., Geels, C., Houweling, S., Imasu, R., Karstens, U., Kawa, S. R., Kleist, J., Krol, M. C., Lin, S.-J., Lokupitiya, R., Maki, T., Maksyutov, S., Niwa, Y., Onishi, R., Parazoo, N., Patra, P. K., Pieterse, G., Rivier, L., Satoh, M., Serrar, S., Taguchi, S., Takigawa, M., Vautard, R., Vermeulen, A. T., and Zhu, Z.: TransCom model simulations of hourly atmospheric CO_2: Experimental overview and diurnal cycle results

20   for 2002, Global Biogeochemical Cycles, 22, 10.1029/2007GB003050, 2008.

Machida, T., Matsueda, H., Sawa, Y., Nakagawa, Y., Hirotani, K., Kondo, N., Goto, K., Nakazawa, T., Ishikawa, K., and Ogawa, T.: Worldwide Measurements of Atmospheric CO_2 and Other Trace Gas Species Using Commercial Airlines, Journal of Atmospheric and Oceanic Technology, 25, 1744-1754, 10.1175/2008JTECHA1082.1, 2008.

Maksyutov, S., Takagi, H., Valsala, V. K., Saito, M., Oda, T., Saeki, T., Belikov, D. A., Saito, R., Ito, A., Yoshida, Y.,

25   Morino, I., Uchino, O., Andres, R. J., and Yokota, T.: Regional CO_2 flux estimates for 2009-2010 based on GOSAT and ground-based CO_2 observations, Atmospheric Chemistry and Physics, 13, 9351-9373, 10.5194/acp-13-9351-2013, 2013.

Maksyutov S., Patra, P. K., Onishi, R., Saeki, T., and Nakazawa, T.: NIES/FRCGC global atmospheric tracer transport model: description, validation, and surface sources and sinks inversion, Journal of Earth Simulator 9, 3-18, 2008.

Manning, A., O'Doherty, S., Jones, A., Simmonds, P., and Derwent, R.: Estimating UK methane and nitrous oxide

30   emissions from 1990 to 2007 using an inversion modeling approach, Journal of Geophysical Research-Atmospheres, 116, 10.1029/2010JD014763, 2011.

Morimoto, S., Nakazawa, T., Aoki, S., Hashida, G., and Yamanouchi, T.: Concentration variations of atmospheric CO2 observed at Syowa Station, Antarctica from 1984 to 2000, Tellus Series B-Chemical and Physical Meteorology, 55, 170-177, 10.1034/j.1600-0889.2003.01471.x, 2003.

Meirink, J., Bergamaschi, P., and Krol, M.: Four-dimensional variational data assimilation for inverse modelling of atmospheric methane emissions: method and comparison with synthesis inversion, Atmospheric Chemistry and Physics, 8, 6341-6353, 10.5194/acp-8-6341-2008, 2008.

Miller, S. M., Saibaba, A. K., Trudeau, M. E., Mountain, M. E., and Andrews, A. E.: Geostatistical inverse modeling with very large datasets: an example from the OCO-2 satellite, Geosci. Model Dev., 13, 1771–1785, 10.5194/gmd-13-1771-2020, 2020.

Nassar, R., Hill, T., McLinden, C., Wunch, D., Jones, D., and Crisp, D.: Quantifying CO_2 Emissions From Individual Power Plants From Space, Geophysical Research Letters, 44, 10045-10053, 10.1002/2017GL074702, 2017.

Necki, J., Schmidt, M., Rozanski, K., Zimnoch, M., Korus, A., Lasa, J., Graul, R., and Levin, I.: Six-year record of atmospheric carbon dioxide and methane at a high-altitude mountain site in Poland, Tellus B, 55, 94-104, 10.1034/j.1600-0889.2003.01446.x, 2003.

Nocedal, J.: Updating Quasi-Newton Matrices With Limited Storage, Mathematics of Computation, 35, 773-782, 10.2307/2006193, 1980.

Oda, T., Maksyutov, S., and Andres, R.: The Open-source Data Inventory for Anthropogenic CO_2, version 2016 (ODIAC2016): a global monthly fossil fuel CO_2 gridded emissions data product for tracer transport simulations and surface flux inversions, Earth System Science Data, 10, 87-107, 10.5194/essd-10-87-2018, 2018.

Parazoo, N. C., Denning, A. S., Berry, J. A., Wolf, A., Randall, D. A., Kawa, S. R., Pauluis, O., and Doney, S. C.: Moist synoptic transport of CO_2 along the mid-latitude storm track, Geophysical Research Letters, 38, 10.1029/2011gl047238, 2011.

Peters, W., Jacobson, A., Sweeney, C., Andrews, A., Conway, T., Masarie, K., Miller, J., Bruhwiler, L., Petron, G., Hirsch, A., Worthy, D., van der Werf, G., Randerson, J., Wennberg, P., Krol, M., and Tans, P.: An atmospheric perspective on North American carbon dioxide exchange: CarbonTracker, Proceedings of the National Academy of Sciences of the United States of America, 104, 18925-18930, 10.1073/pnas.0708986104, 2007.

Peterson, J. T., Komhyr, W. D., Waterman, L. S., Gammon, R. H., Thoning, K. W., and Conway, T. J.: Atmospheric CO_2 variations at Barrow, Alaska, 1973–1982, Journal of Atmospheric Chemistry, 4, 491-510, 10.1007/bf00053848, 1986.

Peylin, P., Law, R., Gurney, K., Chevallier, F., Jacobson, A., Maki, T., Niwa, Y., Patra, P., Peters, W., Rayner, P., Rodenbeck, C., van der Laan-Luijkx, I., and Zhang, X.: Global atmospheric carbon budget: results from an ensemble of atmospheric CO_2 inversions, Biogeosciences, 10, 6699-6720, 10.5194/bg-10-6699-2013, 2013.

Ramonet, M., Ciais, P., Aalto, T., Aulagnier, C., Chevallier, F., Cipriano, D., Conway, T. J., Haszpra, L., Kazan, V., Meinhardt, F., Paris, J.-D., Schmidt, M., Simmonds, P., Xueref-Rémy, I., and Necki, J. N.: A recent build-up of atmospheric CO_2 over Europe. Part 1: observed signals and possible explanations, Tellus B, 62, 1-13, 10.1111/j.1600-0889.2009.00442.x, 2010.

5 Rigby, M., Manning, A., and Prinn, R.: Inversion of long-lived trace gas emissions using combined Eulerian and Lagrangian chemical transport models, Atmospheric Chemistry and Physics, 11, 9887-9898, 10.5194/acp-11-9887-2011, 2011.

Rodenbeck, C., Houweling, S., Gloor, M., and Heimann, M.: Time-dependent atmospheric CO_2 inversions based on interannually varying tracer transport, Tellus Series B-Chemical and Physical Meteorology, 55, 488-497, 10.1034/j.1600-

10 0889.2003.00033.x, 2003.

Rodenbeck, C., Gerbig, C., Trusilova, K., and Heimann, M.: A two-step scheme for high-resolution regional atmospheric trace gas inversions based on independent models, Atmospheric Chemistry and Physics, 9, 5331-5342, 2009.

Rodenbeck, C.: Estimating CO_2 sources and sinks from atmospheric concentration measurements using a global inversion of atmospheric transport, Technical Reports - MPI Biogeochemistry, 6, 53 pp, 2005.

15 Running, S., Nemani, R., Heinsch, F., Zhao, M., Reeves, M., and Hashimoto, H.: A continuous satellite-derived measure of global terrestrial primary production, Bioscience, 54, 547-560, 10.1641/0006-3568(2004)054[0547:ACSMOG]2.0.CO;2, 2004.

Saito, M., Ito, A., and Maksyutov, S.: Optimization of a prognostic biosphere model for terrestrial biomass and atmospheric CO_2 variability, Geosci. Model Dev., 7, 1829-1840, 10.5194/gmd-7-1829-2014, 2014.

20 Schmidt, M., Graul, R., Sartorius, H., and Levin, I.: The Schauinsland CO_2 record: 30 years of continental observations and their implications for the variability of the European CO_2 budget, Journal of Geophysical Research: Atmospheres, 108, 10.1029/2002jd003085, 2003.

Schuh, A. E., Denning, A. S., Corbin, K. D., Baker, I. T., Uliasz, M., Parazoo, N., Andrews, A. E., and Worthy, D. E. J.: A regional high-resolution carbon flux inversion of North America for 2004, Biogeosciences, 7, 1625–1644,

25 https://doi.org/10.5194/bg-7-1625-2010, 2010.

Schuh, A., Lauvaux, T., West, T., Denning, A., Davis, K., Miles, N., Richardson, S., Uliasz, M., Lokupitiya, E., Cooley, D., Andrews, A., and Ogle, S.: Evaluating atmospheric CO_2 inversions at multiple scales over a highly inventoried agricultural landscape, Global Change Biology, 19, 1424-1439, 10.1111/gcb.12141, 2013.

Shirai, T., Ishizawa, M., Zhuravlev, R., Ganshin, A., Belikov, D., Saito, M., Oda, T., Valsala, V., Gomez-Pelaez, A. J.,

30 Langenfelds, R., and Maksyutov, S.: A decadal inversion of CO_2 using the Global Eulerian-Lagrangian Coupled

Atmospheric model (GELCA): sensitivity to the ground-based observation network, Tellus Series B-Chemical and Physical Meteorology, 69, 10.1080/16000889.2017.1291158, 2017.

Stephens, B. B., Miles, N. L., Richardson, S. J., Watt, A. S., and Davis, K. J.: Atmospheric CO_2 monitoring with single-cell NDIR-based analyzers, Atmos. Meas. Tech., 4, 2737-2748, 10.5194/amt-4-2737-2011, 2011.

5   Stohl, A., Forster, C., Frank, A., Seibert, P., and Wotawa, G.: Technical note: The Lagrangian particle dispersion model FLEXPART version 6.2, Atmospheric Chemistry and Physics, 5, 2461-2474, 10.5194/acp-5-2461-2005, 2005.

Stohl, A., Seibert, P., Arduini, J., Eckhardt, S., Fraser, P., Greally, B., Lunder, C., Maione, M., Muhle, J., O'Doherty, S., Prinn, R., Reimann, S., Saito, T., Schmidbauer, N., Simmonds, P., Vollmer, M., Weiss, R., and Yokouchi, Y.: An analytical inversion method for determining regional and global emissions of greenhouse gases: Sensitivity studies and application

10   to halocarbons, Atmospheric Chemistry and Physics, 9, 1597-1620, 2009.

Sweeney, C., Karion, A., Wolter, S., Newberger, T., Guenther, D., Higgs, J. A., Andrews, A. E., Lang, P. M., Neff, D., Dlugokencky, E., Miller, J. B., Montzka, S. A., Miller, B. R., Masarie, K. A., Biraud, S. C., Novelli, P. C., Crotwell, M., Crotwell, A. M., Thoning, K., and Tans, P. P.: Seasonal climatology of CO_2 across North America from aircraft measurements in the NOAA/ESRL Global Greenhouse Gas Reference Network, Journal of Geophysical Research:

15   Atmospheres, 120, 5155-5190, 10.1002/2014JD022591, 2015.

Takahashi, T., Sutherland, S., Wanninkhof, R., Sweeney, C., Feely, R., Chipman, D., Hales, B., Friederich, G., Chavez, F., Sabine, C., Watson, A., Bakker, D., Schuster, U., Metzl, N., Yoshikawa-Inoue, H., Ishii, M., Midorikawa, T., Nojiri, Y., Kortzinger, A., Steinhoff, T., Hoppema, M., Olafsson, J., Arnarson, T., Tilbrook, B., Johannessen, T., Olsen, A., Bellerby, R., Wong, C., Delille, B., Bates, N., and de Baar, H.: Climatological mean and decadal change in surface ocean pCO_2, and

20   net sea-air CO_2 flux over the global oceans, Deep-Sea Research Part Ii-Topical Studies in Oceanography, 56, 554-577, 10.1016/j.dsr2.2008.12.009, 2009.

Takahashi, T., Sutherland, S. C., and Kozyr, A.: Global Ocean Surface Water Partial Pressure of CO_2 Database: Measurements Performed During 1957–2016 (LDEO Database Version 2016) (NCEI Accession 0160492) Version 3.3., Information, N. N. C. f. E. (Ed.), NOAA National Centers for Environmental Information, 2017.

25   Tarantola, A.: Inverse Problem Theory and Methods for Model Parameter Estimation, Inverse Problem Theory and Methods for Model Parameter Estimation, SIAM, 2005.

Thoning, K. W., Tans, P. P., and Komhyr, W. D.: Atmospheric carbon dioxide at Mauna Loa Observatory: 2. Analysis of the NOAA GMCC data, 1974–1985, Journal of Geophysical Research: Atmospheres, 94, 8549-8565, 10.1029/JD094iD06p08549, 1989.

Uglietti, C., Leuenberger, M., and Brunner, D.: European source and sink areas of CO_2 retrieved from Lagrangian transport model interpretation of combined O_2 and CO_2 measurements at the high alpine research station Jungfraujoch, Atmos. Chem. Phys., 11, 8017-8036, 10.5194/acp-11-8017-2011, 2011.

Valsala, V., and Maksyutov, S.: Simulation and assimilation of global ocean pCO_2 and air-sea CO_2 fluxes using ship observations of surface ocean pCO_2 in a simplified biogeochemical offline model, Tellus Series B-Chemical and Physical Meteorology, 62, 821-840, 10.1111/j.1600-0889.2010.00495.x, 2010.

van der Laan, S., Neubert, R. E. M., and Meijer, H. A. J.: A single gas chromatograph for accurate atmospheric mixing ratio measurements of CO_2, CH_4, N_2O, SF_6 and CO, Atmos. Meas. Tech., 2, 549-559, 10.5194/amt-2-549-2009, 2009.

van Leer, B.: Towards the ultimate conservative difference scheme. IV. A new approach to numerical convection, Journal of Computational Physics, 23, 276-299, 10.1016/0021-9991(77)90095-X, 1977.

Vermeulen, A. T., Eisma, R., Hensen, A., and Slanina, J.: Transport model calculations of NW-European methane emissions, Environmental Science & Policy, 2, 315-324, https://doi.org/10.1016/S1462-9011(99)00021-0, 1999.

Vermeulen, A. T., Hensen, A., Popa, M. E., van den Bulk, W. C. M., and Jongejan, P. A. C.: Greenhouse gas observations from Cabauw Tall Tower (1992–2010), Atmos. Meas. Tech., 4, 617-644, 10.5194/amt-4-617-2011, 2011.

Wahba, G., and Wendelberger, J.: Some New Mathematical-Methods For Variational Objective Analysis Using Splines And Cross Validation, Monthly Weather Review, 108, 1122-1143, 10.1175/1520-0493(1980)108<1122:SNMMFV>2.0.CO;2, 1980.

Wang, F., Maksyutov, S., Tsuruta, A., Janardanan, R., Ito, A., Sasakawa, M., Machida, T., Morino, I., Yoshida, Y., Kaiser, J. W., Janssens-Maenhout, G., Dlugokencky, E. J., Mammarella, I., Lavric, J. V., and Matsunaga, T.: Methane Emission Estimates by the Global High-Resolution Inverse Model Using National Inventories, Remote Sensing, 11, 2489, 2019.

Ware, J., Kort, E. A., Duren, R., Mueller, K. L., Verhulst, K., and Yadav, V.: Detecting Urban Emissions Changes and Events With a Near-Real-Time-Capable Inversion System, Journal of Geophysical Research: Atmospheres, 124, 5117-5130, 10.1029/2018jd029224, 2019.

Wheeler, D., and Ummel, K.: Calculating CARMA: Global Estimation of CO_2 Emissions From the Power Sector, 2008.

Worthy, D. E. J., Higuchi, K., and Chan, D.: North American influence on atmospheric carbon dioxide data collected at Sable Island, Canada, Tellus B: Chemical and Physical Meteorology, 55, 105-114, 10.3402/tellusb.v55i2.16731, 2003.

Wu, K., and Simon, H.: Thick-restart Lanczos method for large symmetric eigenvalue problems, SIAM Journal on Matrix Analysis and Applications, 22, 602-616, 10.1137/S0895479898334605, 2000.

Zhuravlev, R. V., Ganshin, A. V., Maksyutov, S. S., Oshchepkov, S. L., and Khattatov, B. V.: Estimation of global CO_2 fluxes using ground-based and satellite (GOSAT) observation data with empirical orthogonal functions, Atmospheric and Oceanic Optics, 26, 507-516, 10.1134/S1024856013060158, 2013.

Figures
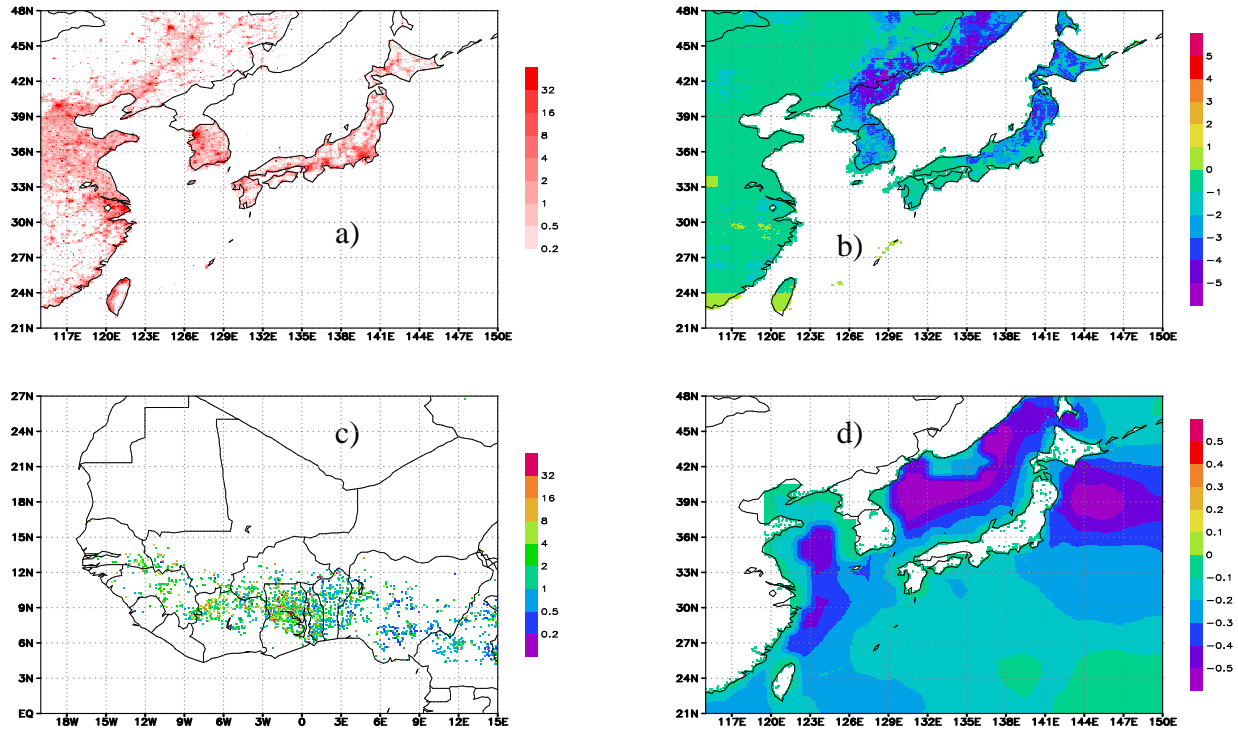
5   **Figure 1: Examples of prior CO₂ fluxes (unit: gCm⁻²day⁻¹): a) emissions from fossil fuel burning by ODIAC (Jan 2011), b) fluxes from terrestrial biosphere by optimized VISIT model (day 160, Jun 9), c) emissions from biomass burning by GFAS in Africa (Jan 10, 2011), d) fluxes due to ocean-atmosphiere exchange by the OTTM assimilation model (Jan 2011)**
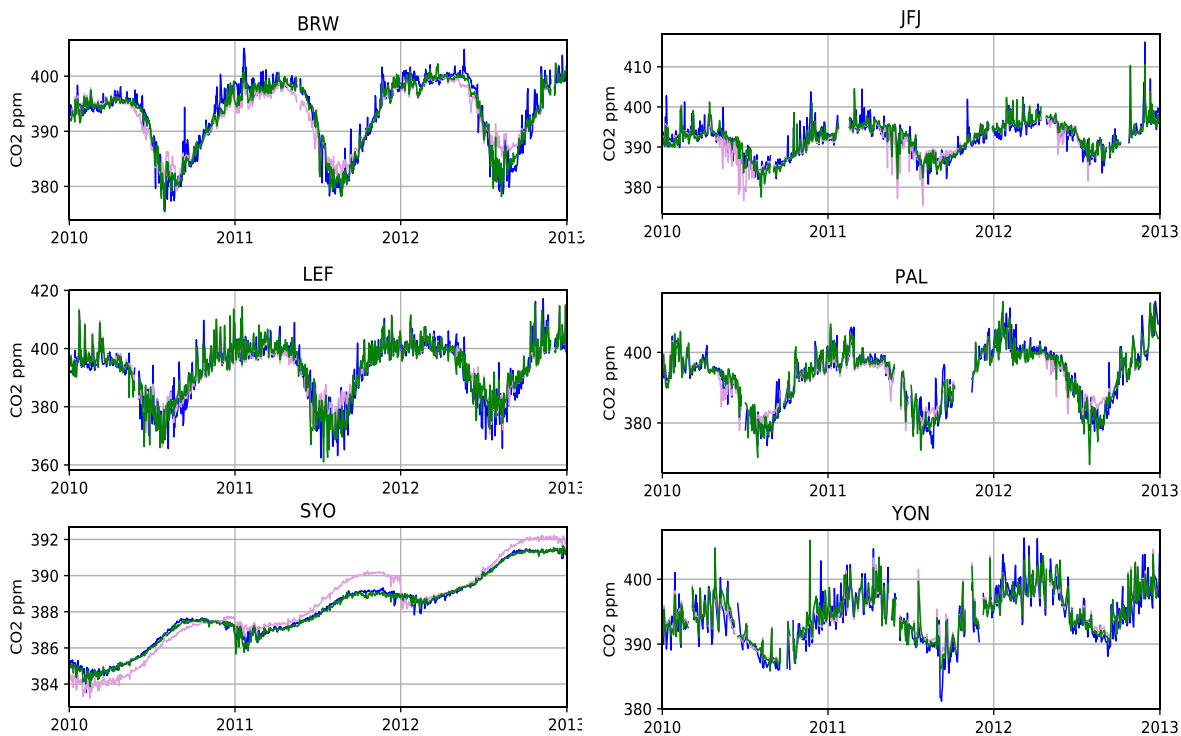
Figure 2: Time series of simulated and observed concentrations (blue - observed, plum -forward (unoptimized), green – optimized) at Barrow (BRW), Jungfraujoch (JFJ), Wisconsin (LEF), Pallas (PAL), Syowa (SYO), and Yonagunijima (YON).
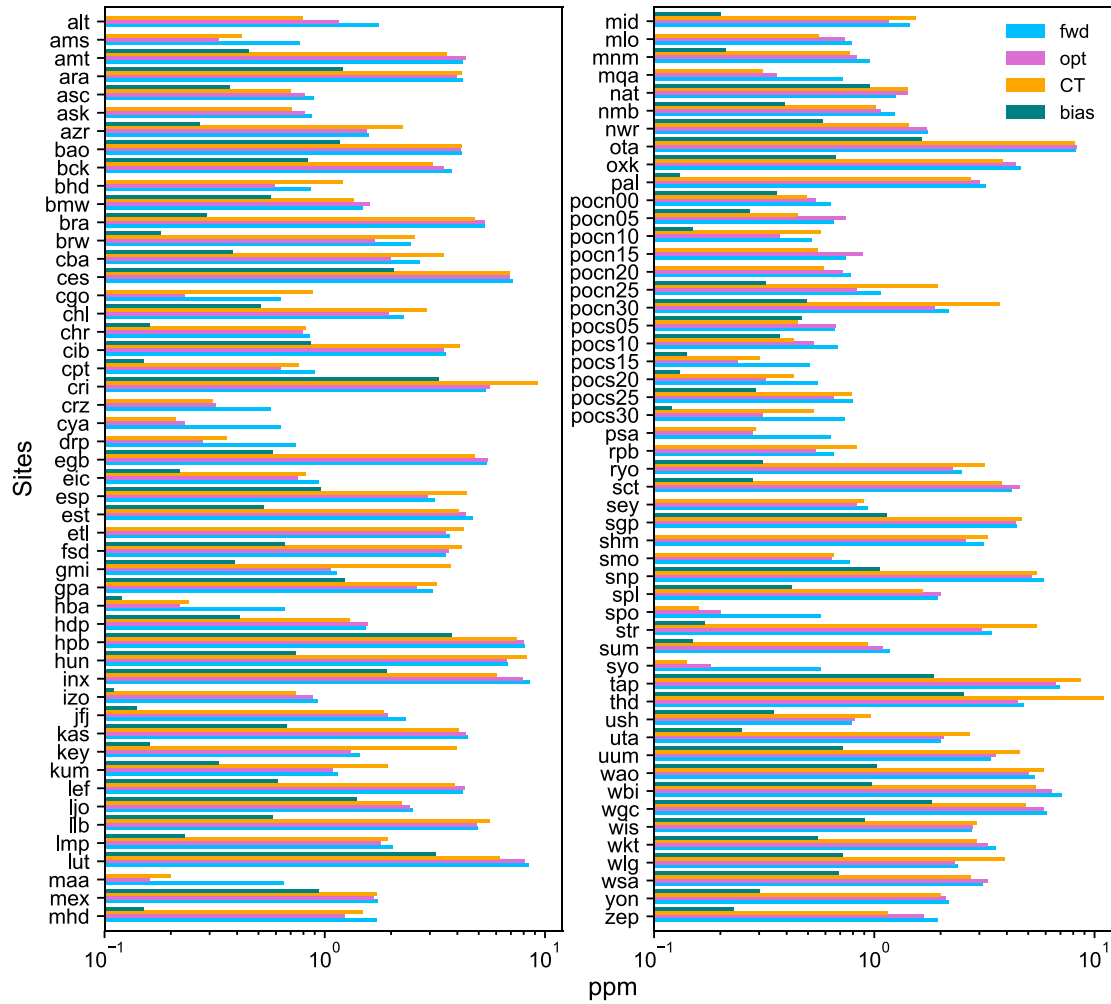
Figure 3: RMS difference between model and observations and absolute bias in 2010-2012 for (surface) sites included in inversion (blue – prior, pink – optimized, orange – CT2017, green – absolute value of mean difference (bias))
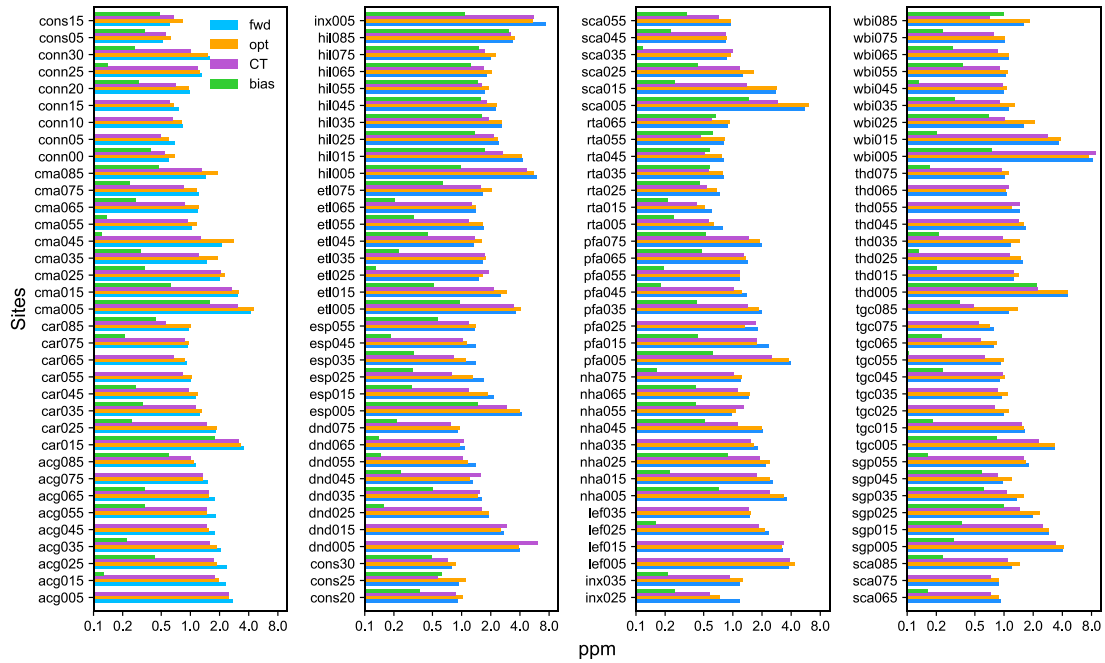
Figure 4: RMS difference between model and observations and absolute bias in 2010-2012 for aircraft sites, not included in inversion (blue – prior, orange – optimized, magenta – CT2017, green – absolute value of mean difference (bias))
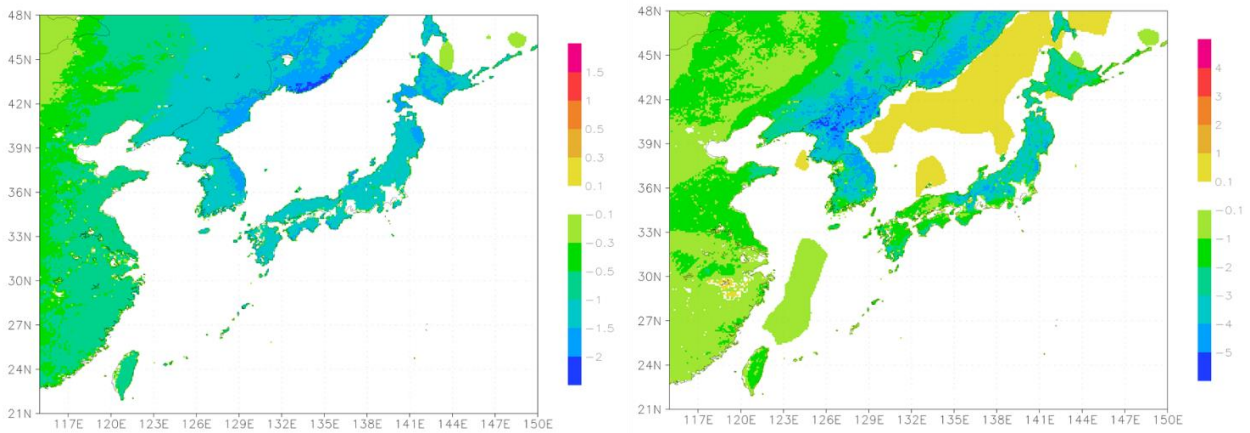
Figure 5: Optimized flux correction (left) and posterior flux (right) maps for August 2011 (units gCm^{-2}day^{-1}, fossil emissions excluded)
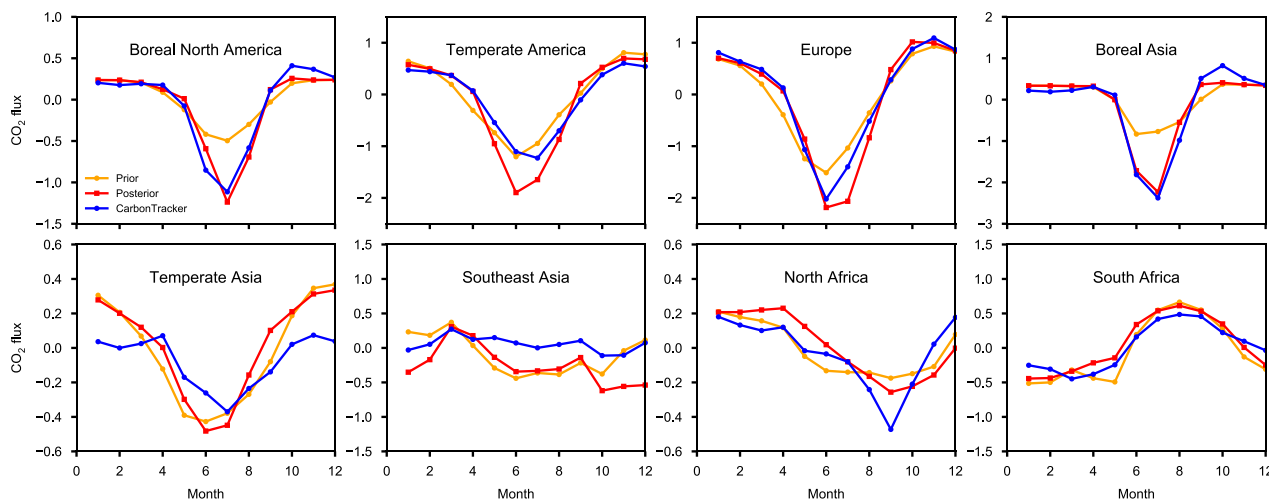
Figure 6: Monthly mean regional fluxes (fossil emissions excluded), average for 2010-2012. Prior, optimized and CarbonTracker for selected Transcom-3 regions (units gCm^{-2}day^{-1}).

Appendix figures.
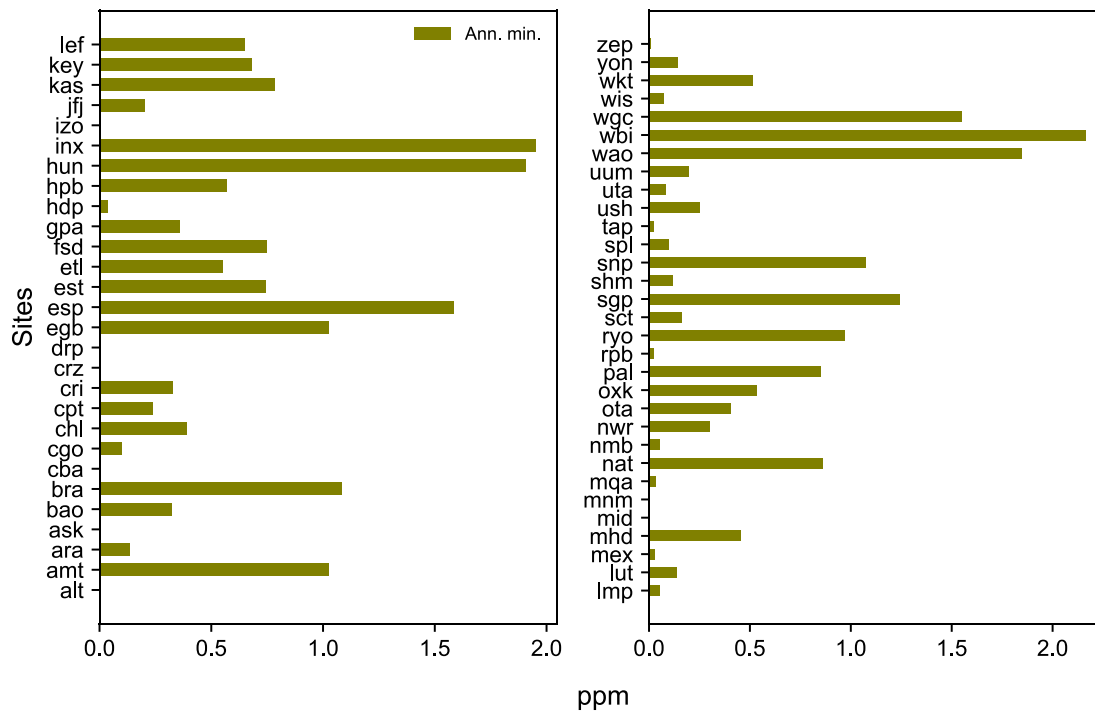
Figure A1: Simulated diurnal cycle bias, 3-month mean in the growing season (units ppm).
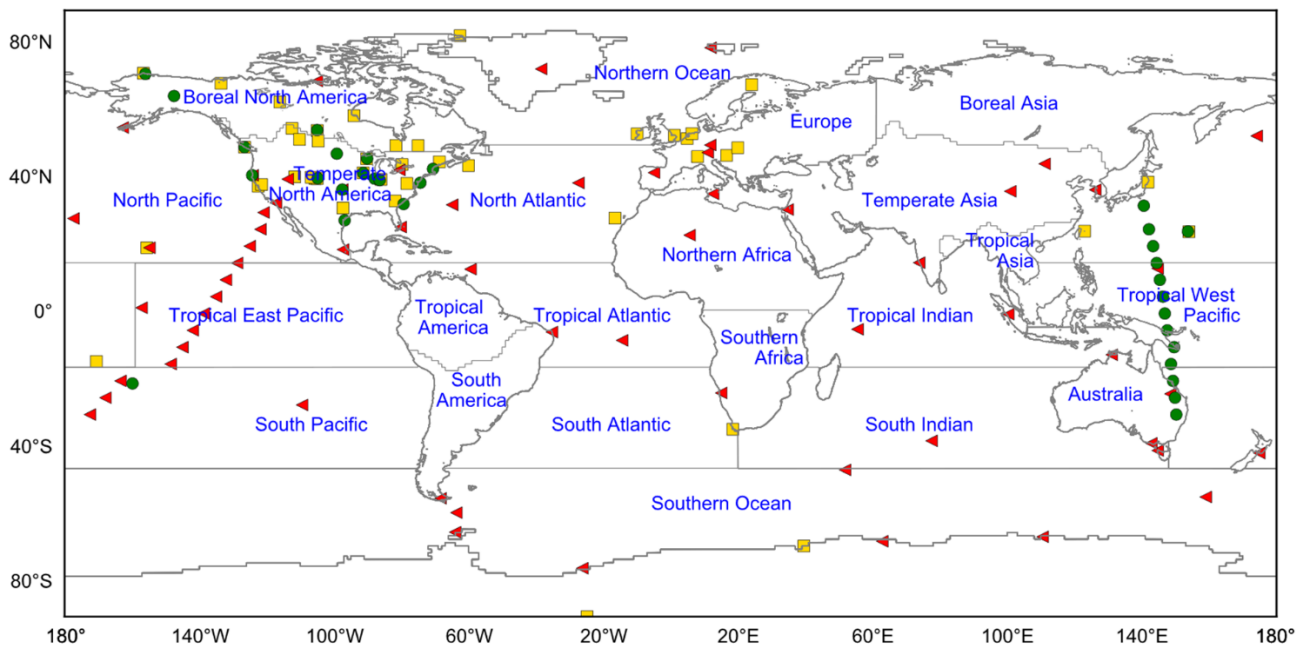
Figure A2: Map of observations sites and Transcom regions (triangles - surface flask sites, squares -continuous, circles – aircraft).
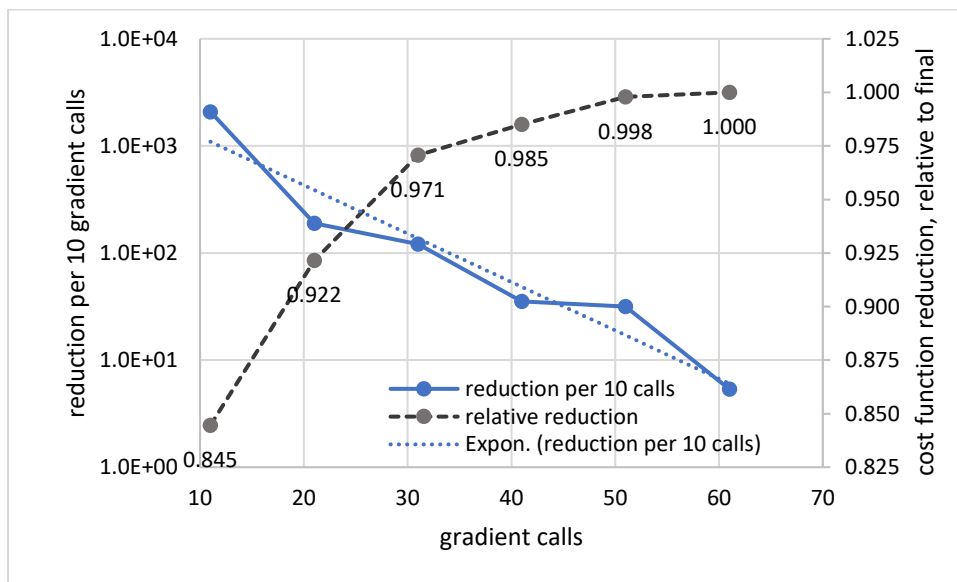
Figure A3: Rate of cost function decline with gradient calls for extended year 2011 inversion and reduction relative to 61 gradient
5 **calls.**